NTNU
Norwegian University of
Science and Technology

Development of a method to determine oxygen distribution in industrial monocrystalline silicon ingots

Joao Manuel Penhaso
Martins

Master's Thesis
Submission date: January 2016
Supervisor: Marisa Di Sabatino, IMTE

Norwegian University of Science and Technology
Department of Materials Science and Engineering

NTNU – Trondheim
Norwegian University of
Science and Technology

Development of a method to determine oxygen distribution in industrial monocrystalline silicon ingots

João Manuel Penhasco Martins

Master's Thesis
Submission date: 21/01/2016
Supervisor: Marisa Di Sabatino, IMTE
Co-supervisor: Yu Hu, NorSun

Norwegian University of Science and Technology
Department of Materials Science and Engineering

Abstract

An alternative method to determine oxygen concentration in industrial monocrystalline silicon has been developed and tested, resorting to statistical analysis and modeling. The model has been applied to different set samples, with a prediction accuracy varying between 90% and 95%. This model works on the assumption of a very effective heat treatment for thermal donor killing and similar thermal history of the produced/analyzed ingots.

List of Abbreviations and Symbols

Abbreviations	**Description**
AHT	After Heat Treatment
BHT	Before Heat Treatment
cm	Centimeter
Cz	Czochralski technique
Cz-Si	Silicon purified by Czochralski technique
FPP	Four Point Probe
FTIR	Fourier Transform Infrared Spectroscopy
FZ	Float Zone technique
Fz-Si	Silicon purified by Float Zone technique
HT	Heat Treatment
mm	Millimeter
Mono-Si	Mono-crystalline Silicon
Poly-Si	Poly-crystalline Silicon
ppma	Parts per Million Atoms
PV	Photovoltaic
R&D	Research and Development

Symbols	**Description**
[C]	carbon concentration
$[O_i]$	Interstitial oxygen Concentration
[TD]	Thermal donor concentration
€	Euro (currency)
Ar	Argon
B	Boron
C	carbon
d	Wafer Thickness
k	Equilibrium Segregation Coefficient
k_{eff}	Effective Segregation Coefficient
L	Position of Ingot
L_0	Ingot Length
NTD	New thermal donor
O	oxygen
O_i	Interstitial oxygen
OTD	Old Thermal Donor
O_{tot}	Total oxygen
P	Phosphorous
q	Elementary Charge
Si	Silicon
T	Temperature
t	Annealing time
TD	Thermal donor
z	Thickness correction factor
$\Delta\rho$	Resistivity Variation
ρ	Resistivity
ρ_0	Resistivity of Seed Wafer

Acknowledgments

For any master's student, the thesis is most likely the most important project one has during its academic course. As for me, the opportunity that was given to me to work, both in a historical university such as NTNU and in a successful company such as NorSun was priceless. Never have I ever thought that I would have such a chance, neither have I thought that it would be such a positive experience, not only professionally, but also for personal development.

Firstly, I would like to give my dearest regards to Professor Marisa Di Sabatino, my supervisor at NTNU, for her invaluable guidance through what was for me a whole new world.

I want to mention the role of Professor João Serra, my supervisor at FCUL, as for without him, I would not have had this chance, and for his useful advice during this project.

My deepest gratitude goes to Yu Hu, my co-supervisor and friend, who guided me through my time in NorSun. Even through a strict schedule, he found the time to assist me and allowed me to find my full potential as a worker.

As my time in NorSun was my first professional experience in the engineering area, I admit I felt, at first, scared. Fortunately, all NorSun's staff was as friendly to me as I could ever wish. I met many great people there and I cannot be any more grateful for all the knowledge I received and for making me feel at home.

For the simulation results, I thank Moez Jomâa.

I would also like to thank Guilherme Gaspar for his advice and help during this work and I wish him the best of luck.

I want to mention the importance of Adeline Lanterne in this work. Her patience, guidance, and advice played a major role, not only in the quality of this thesis but also in my own well-being.

Of course, I also want to thank my family and friends.

Table of Contents

List of Figures

List of Tables

1. Introduction and motivation

PV has shown an overall growth and increasing market share for the last decade [1]. However, the price of this technology is still not low enough to be competitive with some other renewable energy technologies and, even most, with the non-renewable energy production systems. It is known that a cost reduction in the production chain tends to lower the final cost per watt of the system. Therefore, industries and energy companies are making efforts towards this point.

Quality control of the cells and wafers is extremely important, especially for the high efficiency monocrystalline cells industries. One of the most important quality control parameters is the concentration of interstitial oxygen. Fourier Transform Infrared (FTIR) spectrometers are expensive apparatus that allow precise oxygen measurements and, therefore, are widely used as quality control procedure.

The concentration of thermal donors (oxygen clusters) depends on the concentration of intrinsic oxygen, temperature and cooling rate. On the other hand, thermal donors affect resistivity. Assuming that the same equipment, with the same production parameters, produces silicon ingots with similar thermal history, it is possible to develop a model that relate the position of the ingot and the resistivity measured, resulting in oxygen values, valid for that specific equipment and production parameters.

Considering the previous points, the motivation of this study is to develop a method that, through resistivity and positions values, is able to return oxygen values, for faster oxygen measurements, without additional equipment requirements, leading to cheaper quality control, thus resulting in a lower end cost of the silicon wafer and of the solar cell itself.

2. PV industry and Norway

World's energy consumption keeps rising and, with it, the demand of energy production systems. Although energy markets are still controlled by fossil fuels, alternative energies gain, for each passing year, more penetration. Environmental issues and human disasters, in pair with the economic instability brought by fossil fuels price fluctuations, have lead, during the last few decades, to a growing investment, from many developed countries, in the investigation and development of new energy production technologies.

Among these new systems, we find photovoltaic (PV) energy. This technology uses semiconductors to convert luminous energy in electricity. Mostly due to the high cost of initial investment, PV still shows no relevant impact in world's total energy production. On the other hand, during the last few years, PV has shown a significant growth [1] and one can predict in fact that, during the next decades, PV will share an equivalent market share compared with, for example, wind energy. This growth is mainly due to the continuous price reduction and increasing technology maturity.

Norway is one of the major world's energy exporter countries, due to its vast hydric resources, fossil fuel and gas reservoirs. It is also worth mentioning that electricity price in Norway is substantially low. It has also a strong experience in extractive metallurgy industry. All these factors have led to the development of PV industry in this country, even against a very weak internal market, justified by the low solar energy density in its area [2].

Norwegian PV enterprises control around 15% of PV global market, mainly in high quality sectors, namely high purity wafers. Specialists explain this success mainly due to the cooperation between industry, high education and government.

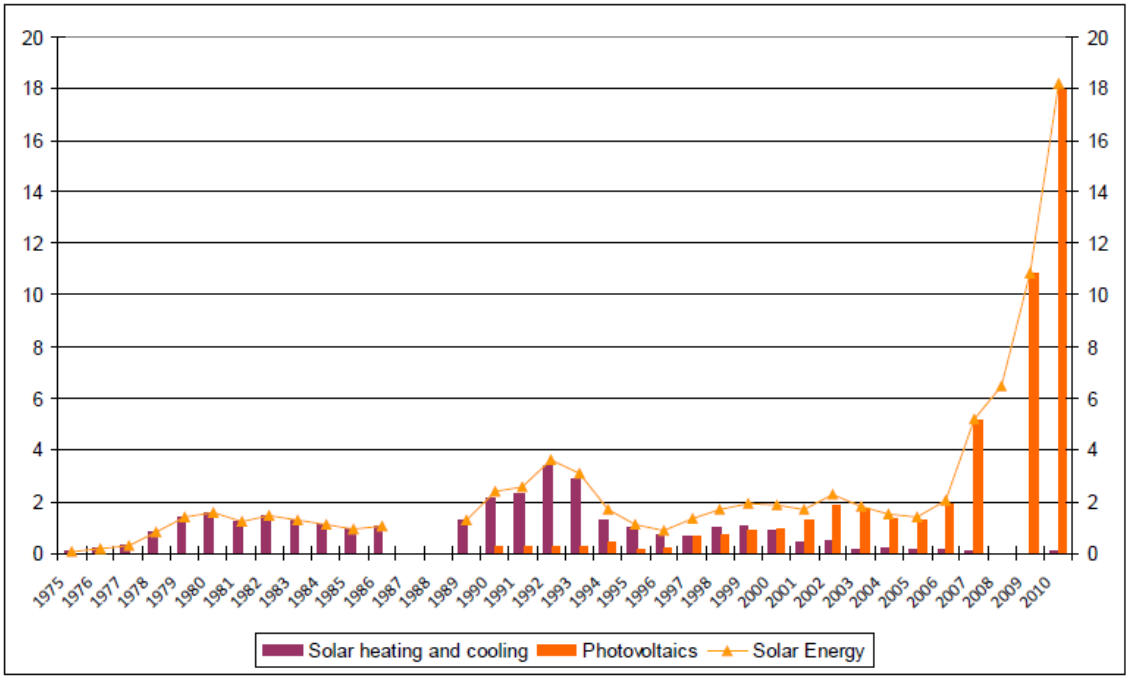

Figure 1: Norwegian public R&D budgets for solar energy during the last decades (million €) [2]. Note the exponential growth in investment in PV R&D during the end of the previous decade.

3. Semiconductors

Semiconductors are materials whose conductivity is between of a conductor (ex: metals) and an insulator (ex: glass) [3]. They are of utmost importance in electronic and photovoltaic technology due to their unique property of being able to either gain or lose electrons, depending of the energy level of the later [6]. Nowadays, silicon is the most common semiconductor, used in various applications due to its enormous availability and, therefore, cheap price [7][3].

A semiconductor material by itself has a very low conductivity due to non-existent flow and electrons and, therefore, no current. This is justified by the fact that a semiconductor is at an electronic equilibrium state [5], that is, its valence bands are already filled [5]. This issue is easily solved through doping.

Doping is the intentional addition of specific impurities to a semiconductor. These impurities will lead to an electronic unbalance in the semiconductor and, therefore, creation of current flow. For PV technologies that use silicon as substrate, the most common intentional impurities, or dopants, are boron and phosphorous. A doped semiconductor is referred as an extrinsic semiconductor, opposed to intrinsic, not doped, semiconductors [3].

To unbalance the electronic equilibrium, is it possible to either raise the number of free electrons or to raise the number of holes. Holes are, in fact, simply a position where an electron could exist. It is easy to understand that this is made possible by adding a dopant that does just

that [4]. As silicon is a group 14 element, as most semiconductors, most common dopants are from either group 13 (as hole donors or electron accepters) or group 15 (as electron donors).

Boron adds electron holes to the crystal lattice of the semiconductor, and since electrons have negative charge, silicon doped with, for example, boron, will accept free electrons and, therefore, will be referred as positive-type silicon, or simply p-type. On the other hand, phosphorous, as it donates electrons, is a negative type dopant and phosphorous doped silicon is referred as n-type silicon. Sometimes, a semiconductor may have both p-type and n-type impurities. In such cases, to classify the type of the semiconductor, one must consider the overall electronic behavior, that is, if it has higher free electron or hole concentration [3].

Electrons and holes can be considered majority or minority carriers, depending of the type of doping. For a p-type semiconductor, such as silicon doped with boron, the concentration of holes is higher than compared with an intrinsic semiconductor. Therefore, holes are considered the majority carriers and electrons are considered the minority carriers. The exact opposite is applied to a n-type semiconductor [13].

As referred above, electron behavior in the crystal lattice of a semiconductor depends of electron energy. This also greatly depends of the material. Each material has what it is called a conduction band and a valence band. Additionally, there is a specific electron energy level called Fermi level, which can be easily put as an energy level that has a 50% chance to be occupied at a time. There is, for most materials, a difference of energy between the energy level of valence and conduction band, denominated as band gap [7].

In metals, since the band gap is nonexistent (or very small for semi-metals), electrons can freely travel from the valence band to the conduction band. As opposite, the band gap for insulators is very high, preventing electron movement from valence to conduction band. An intrinsic semiconductor has a sufficiently small band gap for electron with a certain energy level to break free from its bound state. Doping the semi-conductor will change the range of this energy level. This allows a conductivity manipulation of a semi-conductor to a certain degree.

The purity and structural perfection of the semiconductor, as well as a homogeneous diffusion of dopants with the wanted concentration, greatly affect its quality. Silicon purification will be analyzed during the next chapter.

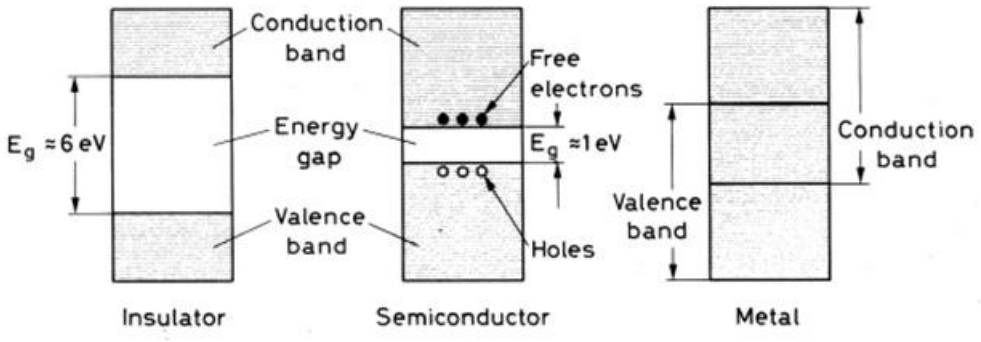

Figure 2: Energy band diagrams for general electric insulators, semiconductors and metals [6].
Eg stands for energy gap, which is the energy that an electron must gain to leave the conduction band and pass to the valence band through the band gap. Metals have no band gap, so any electron can freely travel between both bands. Insulators, on the other hand, have a too large band gap to allow electrons to travel from one band to another. Finally, semiconductors have the propriety of having a band gap sufficiently small to allow electrons within a certain energy level to move to the valence band.

4. Silicon crystal

Although silicon it is rarely found in its pure form in nature, it is in fact the second most abundant element on the earth's crust. Since scale economies are based on the availability of its industry feedstock, this abundance is extremely important for PV to be cost competitive, as this is one of the reasons why both poly-Si and mono-Si are nowadays the most mature and dominant PV technologies.

Besides its huge role in photovoltaic industry, silicon has a series of other industrial applications, such as alloys, ceramics and electronics [8]. Each application needs a specific silicon purity range. This latter application played a major role for PV development because electronic industry requires very pure silicon and, therefore, there has been already, during the last few decades, a strong research and development context for silicon purifying processes. Besides that, for early PV industry, electronic waste was recycled in order to salvage purified silicon.

During the passing years, PV demand and, therefore, industry, grew and, to be cost competitive, it would need to respect an economy of scale pattern, which cannot happen if its feedstock is mainly recycled from a different industry. It was of major importance to develop PV's own silicon purification processes, starting from electronic silicon purifying methods and adapt them to each technology and demand evolution.

Silicon solar cells (either mono crystalline or poly crystalline) are the main PV technology, with a huge market share compared with any other PV technology. This is due to its technologic maturity and decent feedstock availability, although silver, one of the main silicon solar cells components, still leads to a high energy price compared with some renewable energy production systems.

The higher the quality of the silicon solar cell, the higher the silicon purity and, therefore, the more expensive and complex are the silicon purifying processes.

Metallurgic grade silicon has a very low purity to be used in photovoltaic technology, but it is actually used as feedstock for polycrystalline silicon, used in Poly-Si cells [15]. The refining process from metallurgic grade to polycrystalline silicon is mainly done using Siemens process, although there are different new alternatives that lead to a cheaper refined material but less pure.

Siemens process basically consists in the deposition of very pure silicon crystallites along silicon seed rods. These crystallites are originated from a silicon compound in gaseous form, such as trichlorosilane ($SiHCL_3$) or silane (SiH_4), at a very high temperature range.

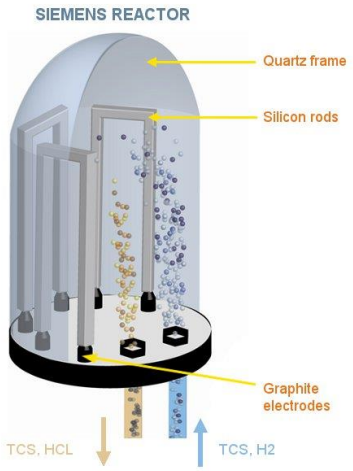

Figure 3: Siemens reactor schematic for poly-Si production [9].

Gaseous molecules containing silicon elements in their constitution are injected in a quartz closed structure. The silicon will be separated from the gas by contacting very hot silicon rods and form crystallites along the rod, resulting in grown multi crystalline ingots.

Poly-Si produced by Siemens process is pure enough to be used in PV, but, since it is constituted by an aggregation of many crystals, crystalline structure losses are very high and it has a lower purity compared with silicon refined by other processes like Czochralski or Float Zone.

Figure 4: Poly-Si solar cell (left) and mono-Si solar cell (right) [10].

Note the clear crystal formations in the poly-Si solar cell versus the homogeneous visual appearance of mono-Si solar cell.

Nonetheless, Poly-Si is used as feedstock for mono-crystalline silicon. Mono-Si wafers have low structure losses since they are cut from one single silicon crystal and have a higher purity than poly-Si. On the other hand, they are much more expensive.

Two main mono-Si processes exist nowadays: Czochralski and float zone. Although float zone offers crystals more pure than Czochralski, the latter is much cheaper and it's a very mature technology.

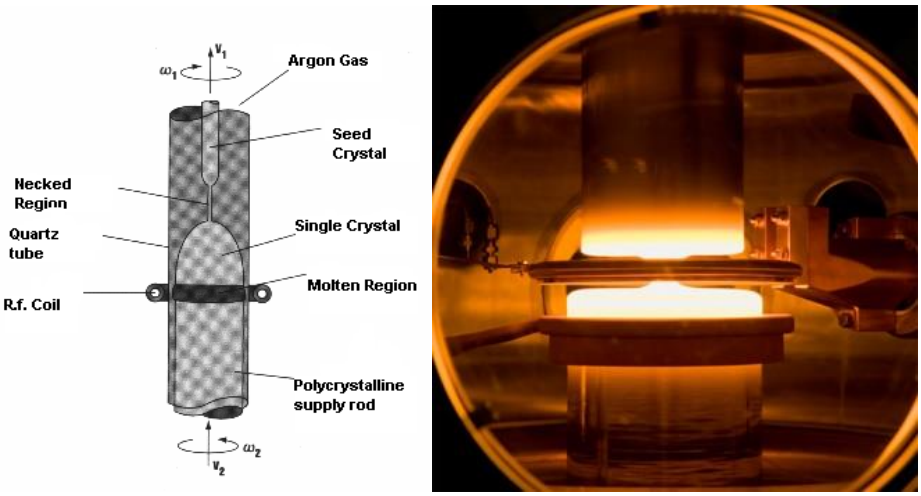

Figure 5 [11]; 6 [12]: schematic of FZ technique (left) and picture of the molten region during FZ process (right).

At inert argon atmosphere, a polycrystalline silicon rod is placed inside the device. Induction coils heat silicon axially in a small length range. Those coils move along the ingot, allowing impurities to segregate to one end of the ingot, resulting in extremely pure crystals. oxygen concentration in FZ-Si is extremely low, since it does not resort on a crucible to contain the silicon melt, which is the main oxygen source of CZ-Si.

5. Czochralski crystal growth

As this thesis approaches Czochralski crystal pullers, it is important to study the current state of this technology, as well as the control systems that alter ingot properties. The basic principle of CZ-Si production is the use polycrystalline silicon as feedstock for a further conversion into a single, very pure crystal.

CZ Puller

The main parts of this apparatus are located in the main vessel, which is a vacuum-proof, water cooled, cylindrical structure made of steel. This structure is insulated to reduce heat losses. Usually, one can find a viewport in this structure to observe the crystal growth. The bottom of this structure contains the electrodes necessary for the power supply of the heaters. It is inside of this chamber where the crucible is placed on a pedestal, which importance will be explained later in this chapter.

The crucible is one of the most important components of CZ-Si production, as it is where the poly-Si feedstock will be placed and melted. Due to its direct contact with this melt, it is one of the major impurity sources [14]. To minimize the incorporation of these impurities, this crucible is made of SiO_2 (quartz) [16]. Due to the high temperatures necessary for poly-Si to melt, the crucible borders dissolves in the melt, resulting in the incorporation of oxygen in the melt and, furthermore, in the final ingot produced. To reduce this issue, the melt temperature should be optimized to a value slightly higher than the melting point of silicon, which is 1412 ºC [45]. If the melt temperature is increased above the optimized point, it may lead to an increase of mechanical stability losses and corrosion [15] and, furthermore, an increase of energy consumption by the device, which obviously is reflected over the final cost.

Above and connected to the main vessel the upper chamber is located. It is in this chamber that the pulling wire (or, in some devices, the pulling shaft) is and, therefore, where the crystal

grows vertically. In some pullers, cooling equipment is positioned along the upper chamber, mainly for impurity control [19].

On the top of the apparatus the pulling unit is placed, which contains a wire or shaft for the pulling process. At the end of this wire of shaft a seed holder is mounted, where the seed crystal is placed. This unit holds the seed near the melt to initiate the crystal formation and, during the solidification, pulls the crystal vertically, along with a rotation movement. The pulling speed greatly controls the ingot diameter [18].

Opposite to the pulling unit, some pullers have a shaft connected to the pedestal. This shaft has the capability of controlling the vertical position of the crucible, as well as adding a rotation movement, usually in the opposite direction of the crystal rotation [16]. The vertical position control is important to control the melt surface with respect to the main heaters and the rotation movement leads to important convection melt flows [23].

To avoid contamination, both the upper chamber and the main vessel are purged with argon. Furthermore, using heat shields, an argon flow is controlled with the purpose of transporting away prejudicial gases for the melt and the crystal, such as silicon monoxide (SiO) [17].

The final major component, with the utmost importance of crystal growth quality and growth process control, is the hot zone, which is simply the set of heaters placed inside the chambers. These heaters are made of solid, very pure graphite. The heat is firstly transferred to a graphite susceptor by radiation, which will uniform heat transfer and, since it is positioned in the pedestal, it gives some mechanical support to the crucible [19].

Nowadays most CZ pullers are semi-automatic, permitting a single technician to operate several pulling stations at a time [14].

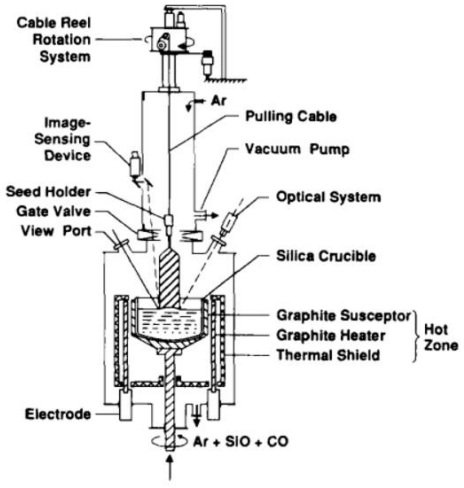

Figure 7: Schematic of CZ puller [20].
Notice the hot zone surrounding the crucible, the crystal and crucible rotation mechanisms and inner chamber gas flows.

CZ crystal growth procedure

The overall operation procedure for crystal growth is similar between all pullers.

Firstly, it is necessary to charge the crucible with feedstock. For CZ-Si, this feedstock is poly-Si, as already referred above. If this poly-Si isn't already highly doped, it is necessary to add very pure dopants, in a very specific quantity, according to the wanted material characteristics. The crucible is then heated to melt the feedstock. The seeding process can't start until the melt temperature has achieved a relative stabilization [16].

The seeding process starts as soon as the melt reaches an optimal steady condition (it is important to refer that this stabilization is never perfect, due to turbulent flows in the melt [23]). The seed is lowered under rotation until it is near the melt, but not in contact, for preheating, to avoid thermal shocks [14]. When the very bottom of the seed is melting and a meniscus between that portion of the seed and the melt surface is formed, the optimal condition previously referred is achieved and the crystal formation starts. Si atoms are rearranged along the meniscus to form a perfect crystalline lattice [18].

The seed is pushed vertically during the necking process. This step is important to avoid the formation of dislocations during the crystal growth. After this point, the pulling speed is decreased, so the diameter of the crystal grows until the wanted value, creating a conic shape referred as the crown or shoulder [17]. When the crystal reaches that optimal diameter value, the pulling speed is stabilized. To control the diameter value, alongside the pulling speed control, the crucible vertical position also changes, so the melt surface is always constant.

When the crystal body reaches the desired length, pulling speed is increased, forming another conic structure: the tail. It is important that the tail reaches a small diameter, otherwise the detachment may cause dislocation in the crystal [23]. There is always some residual melt left in the crucible. To detach the crystal from this residual melt, the pulling speed increases to the point where the crystal leaves the contact with the melt, but slow enough to avoid too strong thermal shocks.

Finally, the crystal is pulled vertically until it is completely within the upper chamber, for cooling. The cooling rate must be controlled to be within a range that will minimize impurities precipitation, such as thermal donors, but avoiding structure losses due to thermal shocks [18].

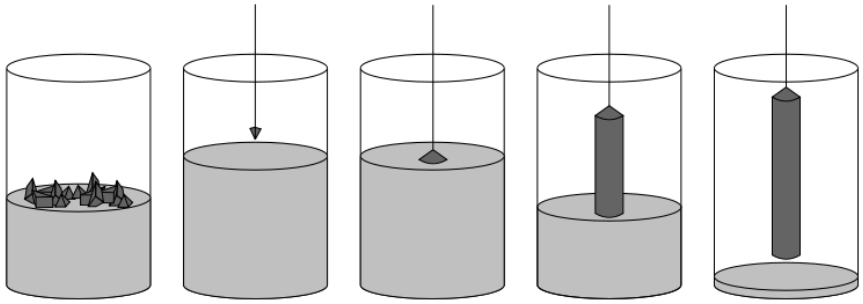

Figure 8: Schematic of CZ crystal growth [21].
Firstly, the melt of the feedstock occurs. After temperature stabilization, the crystal seed is lowered and the necking starts. After the body of the crystal is fully grown, the ingot is slowly detached, forming the tail.

6. Impurities

Impurities in Si wafers greatly influence solar cell performance, with both positive and negative outcomes. For Czochralski process, the most important impurities are the dopants, oxygen and carbon [24]. Due to the topic of this thesis, thermal donors, which are in fact directly related to oxygen, will also be addressed.

The concentration of any impurity may vary along the ingot, both in axial and in radial direction, leading to wafers with different quality. To produce optimal wafers it is important to understand why and how these variations occur.

Impurities present in the melt will segregate into the material during the solidification. For most materials (such as alloys or crystals) and for most impurities, it is possible to find the concentration of a specific impurity present in the solid interface using the Scheil's Equation [27]:

$$\frac{C_s}{C_0} = k_0(1 - f_s)^{k_0 - 1}$$

C_s is the concentration of an impurity in the solid, k_0 is the equilibrium segregation coefficient, C_0 is the initial concentration in the melt and f_s is the fraction of the solidified part.

For this equation to be reasonably true, there are a few assumptions that must be respected: 1. There is no diffusion in the solid; 2. Diffusion in the liquid is instantaneous; 3. Solid-liquid interface is at an equilibrium; 4. Solidus and liquidus lines are straight segments [30].

One can analyze the equation and easily understand that, for $k_0 < 1$, impurity concentration increases along the length of the ingot. Most impurities that affect CZ-Si have, in fact, a k_0 lower than one, with the exception of oxygen, which has a $k_0 \approx 1$ [25].

In respect to CZ-Si, the first and fourth assumptions are well respected due to the crystal lattice chemical and mechanical characteristics. The second assumption may be or not respected, depending mostly of the diffusion coefficient of the respective impurity (that is, for impurities with a very low diffusion coefficient, such as carbon, this assumption is not respected and, therefore, it is not possible to apply Scheil's Equation to estimate carbon concentration). The third assumption is not always perfectly met, but can be reasonably corrected if the effective segregation coefficient, $k_{eff,}$ is used instead of using the equilibrium segregation coefficient. k_{eff} depends on the equilibrium segregation coefficient, crystal rotation speed ω, growth rate f, kinematic viscosity υ, diffusion coefficient D, as it follows [28]:

$$k_{eff} = \frac{k_0}{k_0 + (1 - k_0)exp(\frac{-1{,}6D^{1/3}\upsilon^{1/6}\omega^{-1/2}f}{D})}$$

Measuring most of the variables needed for the calculation of the effective segregation coefficient is not trivial. In fact, the best solution to find this parameter is actually resorting to iterative processes.

As referred before, impurity concentration in the center of the ingot is not always similar to the impurity concentration in the periphery, for the same axial value. It is known that this axial variation is dependent of the position and thermal history and control parameters, such as a high

crystal rotation and optimal crucible rotation. Although not critical, axial variation may still lead to structure issues and loss of total efficiency of the solar cell [25].

Dopants

Dopants are added impurities to the crystal constitution that will change the semiconductor electronic proprieties. Most common dopants in CZ-Si are boron (for p-type silicon) and phosphorous (for n-type silicon). One of the most important proprieties of these dopants is that dopant atoms replace silicon atoms in the crystal lattice, if added during crystal solidification. This leads to a change of electronic proprieties of the resulting wafers without structure degradation [22].

Dopant concentration is very controlled, although it varies along the length of the ingot. It is also very dependent of the application and client requirements for the end wafers, but is typically between $5*10^{12}$ and $5*10^{19}$ atoms per cm^3.

Dopant concentration and, therefore, resistivity, usually increases along the radius of the ingot, with phosphorous showing a higher radial variation than boron, due to the lower equilibrium segregation coefficient [29].

It is known that dopant concentration reflects in unwanted impurity concentration. For example, highly doped ingots will tendentiously have considerably higher intrinsic oxygen content, when compared with lightly doped ingots produced using similar parameters [25].

Oxygen

Due to the dissolution of the SiO_2 crucible walls in the melt during Czochralski crystal growth, high oxygen incorporation in the crystal lattice is to be expected. Due to this relatively high concentration, oxygen plays a major role in wafer quality, as the most prejudicial impurity [26].

It is possible to control oxygen dissolution in the melt and, furthermore, oxygen segregation into the crystal, through crucible and crystal rotation, in unity with the thermal convection phenomena occurring both in the melt and in the atmosphere that surrounds it. SiO is very volatile, so a great percentage of evaporated SiO is pushed further away through argon forced flow. The following equation shows the formation of SiO, in gaseous form, through the reaction that occurs between the SiO_2 found in the crucible and the Si found in the melt [32]:

$$SiO_2 + Si \longrightarrow 2SiO$$

Typical oxygen concentration in CZ-Si crystals is between $2*10^{17}$ and $1*10^{18}$ cm^{-3} and it greatly varies along ingot length [25]. The Scheil's equation cannot predict oxygen concentration due to the oxygen evaporation from the melt and the oxygen addition to the melt through crucible walls dissolution. Therefore, one can easily conclude that oxygen concentration along the ingot length presents a very high dependence over the crucible characteristics and process parameters

The control mechanisms mentioned earlier not only influence oxygen concentration along the length of the ingot, but also along the radius of the ingot. As difficult as it is to control oxygen

concentration along an ingot, is even more complex to reduce oxygen radial gradient, mostly due to the turbulent behavior of the melt.

Understanding the oxygen diffusion coefficient is of utmost importance in order to analyze oxygen aggregation and, therefore, thermal donors, which will be address in the subchapter. Oxygen diffusion coefficient is greatly influenced by temperature, respecting the following equation [30]:

$$D_{OXY} = \frac{a_0^2}{8\tau} * \exp(-\frac{E_D}{kT})$$

D_{OXY} is oxygen diffusion coefficient ($cm^2\ s^{-1}$), a_0 is lattice spacing of Si, with a constant value of 5,42Å, τ is the mean lifetime, E_D is the activation energy, k is the Boltzmann constant and T is temperature. High oxygen diffusion leads to lower oxygen agglomeration. Analyzing the equation will reveal that the agglomeration phenomena will occur more frequently at lower temperatures. This is one of the reasons of the importance of the cooling process control of a CZ-Si ingot.

Oxygen content in CZ-Si is responsible of a great number of defects. Oxygen precipitates lead to slip generation, causing structure losses and degradation of wafer quality. Oxygen precipitation may also result in oxygen-induced stacking faults (OISF), lowering wafer surface perfection. Besides these structure loss examples, oxygen may also influence the electrical proprieties of the semiconductor [25]. This phenomenon will be addressed in the following chapter.

Thermal Donors

Thermal Donors (TDs) are electrically active clusters of oxygen. They highly influence the electrical proprieties of the semiconductor, since they act as electron donors, changing the carrier concentration. For p-type crystals, thermal donors will reduce carrier concentration and, therefore, increasing resistivity. The opposite effect occurs for n-type crystals. Although TDs do not have a direct affect in the efficiency of the solar cell, they lead to lower lifetimes [32].

TDs are formed during crystal cooling due to interstitial oxygen precipitation. There are many different species, although it is possible to classify them in two different types: old thermal donors (OTD) and new thermal donors (NTD).

NTD have a positive relation with carbon concentration and they are formed at a temperature range of 650ºC to 800ºC. This group of species is, in fact, less relevant than OTD, since its concentration is much lower. On the other hand, OTD are formed at lower temperatures, between 300ºC and 500ºC, with a much higher formation rate and, therefore, a higher concentration [35]. In fact, TDs concentration decreases along the ingot, resulting in higher concentration values near the seed when compared to near tail positions, due to a longer exposure time to low temperature.

The concentration of TD has a very close relation with intrinsic oxygen concentration. The following equation explains the formation of oxygen agglomerates and SiO_2 precipitation (I stands for interstitial configuration) in CZ-Si [30]:

$$2xO_I + ySi \leftrightharpoons xSiO_2 + (y - x)Si_I$$

As one can observe, higher Si_I content leads to precipitation retarding, and the equation shifts its direction to the left, resulting in intrinsic oxygen agglomerates. Furthermore, it is possible to express thermal donor concentration through the following law [32]:

$$[TD] = k_t([O_i]\ (1 + \frac{2}{3}D_i t[O_i]^{\frac{2}{3}})^{-\frac{2}{3}})^n t^{1,02}$$

Where k_t is a constant valuing $4{,}61*10^{-52}$, *Di* is oxygen diffusion coefficient, *t* is annealing time and *n* is a power dependency factor. Increasing annealing temperature lead to increasing oxygen atoms incorporated in thermal donor center, leading to a power dependency that varies with temperature.

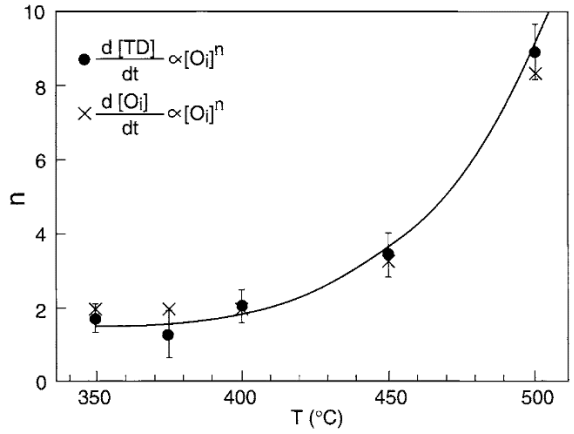

Figure 9: Power dependency n of TD formation (circles) and loss of Oi atoms (crosses) versus annealing temperature [31].

As complex as the previous law may be, all its parameters are either fixed constants or functions that are mostly dependent of annealing time and/or temperature. Therefore, one can express TD concentration through a function that is only dependent of oxygen concentration, annealing time and temperature:

$$[TD] = f([Oi],\ t,\ T)$$

Leading to the conclusion that thermal donor concentration can be expressed, in fact, by oxygen concentration and thermal history, although there has not been found a correlation between oxygen concentration and thermal donors at low temperatures during previous studies [34]. This important point and will be address latter, as it is the basis of this thesis topic.

TDs act as double donors, that is, each TD may donate two electrons. As referred above, this leads to a very direct impact in the resistivity ρ:

$$\rho = (q * \mu_p * p + 2 * [TD])^{-1} \text{ for p-type semiconductors}$$

$$\rho = (q * \mu_n * n + 2 * [TD])^{-1} \text{ for n-type semiconductors}$$

Where q is elementary charge, μ_p is hole mobility, μ_n electron mobility, p is dopant concentration of the p-type semiconductor and n is dopant concentration of the n-type semiconductor [25]. This effect in the material resistivity is a serious issue to wafer quality. In fact, the type of the semiconductor may even change due to thermal donors, if lightly doped.

Fortunately, thermal donors can be destroyed resorting to a heat treatment process. By raising wafer temperature until a certain value, during a related time, thermal donors will be eliminated. Further cooling to room temperature in a short period will prevent thermal donor reformation, leading to normal resistivity values.

Carbon

Carbon is the second most relevant unwanted impurity contained in CZ-Si. Although found with relatively low concentrations values (typically below $2{,}5*10^{16}$ atoms/cm^3), it enhances oxygen precipitation and, at higher concentrations, may lead to structure loss [25].

Although the feedstock used in the melt may contain carbon that will contaminate CZ-Si crystal, the most important carbon source is the graphite material in the hot zone. Evaporated SiO from the crucible reaches the graphite, resulting in the following reaction [30]:

$$SiO + 2C \longrightarrow SiC + CO$$

CO will be part of melt composition and may be part of crystal composition. Since this reaction continuously occurs along ingot solidification and, therefore, carbon content is continuously added to the melt, it is not possible to use Scheil's Equation to estimate carbon concentration values [17]. Nonetheless, it is possible to conclude that it will generally increase along the length of the ingot.

7. Sample preparation

The 129 samples used were produced and donated by NorSun, along with additional data about ingot proprieties and seed and tail wafers proprieties. Each ingot that NorSun produces results in 4 to 6 blocks. Each test sample results, therefore, from each block of a specific ingot. This results in a large set of data for a very short length range, divided in five different main sets. This point will be address later. It is also important to refer that different pullers and different run parameters were used to create the ingots that originated these samples. Nonetheless, a certain similarity is assumed. Additional data over the production characteristics of each ingot has been granted, allowing the direct comparison of a small number of samples that were originated by the same equipment and run parameters.

All test wafers were already cut and lightly polished. As chemical etching is not part of the standard procedure anymore, it was decided that a simple surface cleaning, using ethanol, would suffice. This simple cleaning was done both before any measurement and after heat treatment. Measures showed significantly different values for the same sample before and after cleaning. Another positive point of this short step is that ethanol, during its evaporation, absorbs heat from the samples. This is especially useful for after heat treatment measures of resistivity values, since temperature variations during the measuring procedure will change the results and the absorbed heat from the evaporated ethanol will lead to faster temperature stabilization and, therefore, more accurate results and faster measuring procedure.

The heat treatment in NorSun consisted in heating the samples at 700ºC during 17 minutes. The cooling process, although not well defined, consisted in the opening of the oven's door and, after a few minutes, the holder containing the samples would be placed near a unidirectional ventilator to force cold air flow, until the samples reached the room temperature.

NTNU's certified heat treatment consisted in heating the samples at 800ºC during 10 seconds. All samples are polished before treatment. The cooling process is completely controlled as well.

To compare the performance of NorSun heat treatment procedure, 2 samples were cut in two. One pair was measured and treated accordingly standard NorSun procedure, while the other pair has been treated and prepared accordingly NTNU standard procedure. This comparison has been carried out due to the suspicion that the heat treatment procedure of NorSun was not optimal, as for the oxygen concentration of the tested samples after heat treatment was substantially lower than before heat treatment, which may be explained by re-precipitation of the oxygen, which may lead to untrustworthy results. This point will be address latter.

The two samples measured in NTNU required preparation, namely mechanical polishing. Since the samples were already lightly polished, the preparatory polish executed with the grinding paper consisted simply in the use of three different cloths with the adequate grain size. The grinding time for each cloth was roughly two minutes. After the removal of particles that may damage the surface of the sample, the final polish procedure would start. For this step, other three different cloths were used with 9 µm, 3 µm and 1 µm of grain size, during a time of 4, 3 and 2 minutes, respectively. Between each polishing step, the sample would be cleaned with ethanol, to avoid particle surface damage. This procedure is the certified standard polishing procedure that is carried out in NTNU.

8. Characterization techniques and methods

During this chapter, relevant information about measurement procedure and used equipment will be explained. This will allow an understanding of the measurement precision and how it affects the final results.

Four Point Probe

This method is used to measure resistivity values. This is achieved using an apparatus that has four aligned tungsten probes [38]. The outer ones apply current and the inner ones measuring voltage. This allows to determine the resistance by applying the Ohm's Law and, therefore, the resistivity, which is defined as:

$$\rho = \frac{RA}{l}$$

Where ρ is resistivity (Ω.cm), R is resistance, A is current and l is the sample thickness.

By using four different probes, assuming they are at a minimum distance from each other, the contact resistance is eliminated, which greatly changes the results of any semiconductor measure.

Resistivity measured with FPP respects the following equation:

$$\rho = \frac{2\pi d U_v}{I_c}$$

Where d is the distance between the probes (standardly with a value of 0,635 mm), U_v is the voltage measured by the inner probes and I_C is the current applied by the outer probes.

Resistivity measures are only true if we assume the sample has a semi-infinite thickness, from the point of view of the apparatus. If a sample is too thin (with a thickness below 5d), a correction factor should applied. Therefore, the final resistivity will be given by multiplying the measure value by the following correction factor [27]:

$$z = \frac{1}{1 + \frac{0{,}52632}{(t/d)^{1{,}9}}}$$

Where z is the correction factor and t is the thickness of the sample.

Resistivity also depends of the temperature. A linear approximation may be used for small variations:

$$\rho = \rho_0(1 + \alpha(T_f - T_0))$$

Where the $\rho 0$ is the measured resistivity, α is the temperature coefficient of resistivity (-0,07 for silicon [45]), T_f is the temperature measured at the end of the measuring and T_0 is the temperature measured in the beginning of the measurement.

To reduce the errors of this relation, only measures with a temperature variation less than 0,5 ºC between the start and the end of the measurement were accepted. As described earlier, ethanol cleaning helped reaching temperature stabilization as well.

The FPP used in NorSun was a 4D 280I model. As read in the equipment specifications, it has a precision of 0,1% [40].

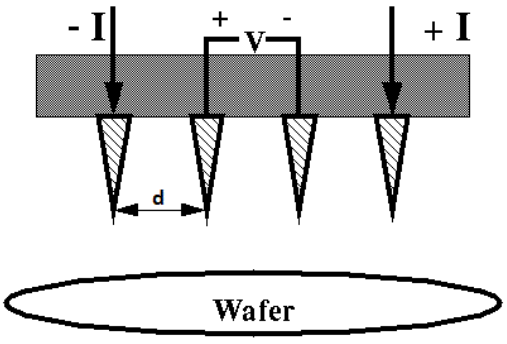

Figure 10: Four Point Probe Schematic [39].
Due to the distance between each probe and due to different pairs of probes used respectively for current appliance and voltage measuring, contact resistance is eliminated, leading to very accurate measures, even for thin samples with low resistance.

FTIR

FTIR stands for Fourier transform infrared spectroscopy. This technique is widely used to analyze many different organic and inorganic materials, since it is a fast, precise and nondestructive measuring method. To study silicon impurities, it is important to resort to FTIR, since it is able to give very accurate data about the major impurities present in the samples.

Although there are different types of spectrometers with additional components, most of the apparatus have a very similar structure and operation method. A source of light creates an infrared laser that passes through a beam-splitter, creating two different beams. One beam will reach a stationary mirror and the other one will reach a moving mirror. Both beams are reflected and will encounter an interferometer, which in turn will return a signal with information about the selected range of frequency, due to the different frequency values originated by the moving mirror, at each instant [43]. This recombined laser will then pass through the sample and finally reach the detector. This signal, after further conversion to digital signal and amplification, will be transferred to a computer, which will automatically process the signal using Fourier Transform [42] and, finally return a frequency spectrum.

Chemical bonds vibrate at certain frequencies when absorbing IR radiation. Therefore, by having the absorption and the frequency of the signal, it is possible to know the concentration of various elements present in the sample, such as oxygen and carbon. It is possible to obtain a spectrum of radiation absorption as function of frequency. The peaks of this spectrum show the impurity concentration for the specific element that matches that frequency. Beer-Lambert law is the relation that makes possible this relation. A simplification of this law is:

$$A = abc$$

Where A is absorbance, a is absorptivity, b is the thickness of the sample and c the concentration of that specific element. This relation can be easily rearranged to return the wanted concentration values [41].

Although FTIR is a very precise technique, certain proprieties of the material may influence the measures. It is know that the absorption by free carriers for samples with a certain range of resistivity will greatly influence the accuracy of FTIR measurements. FTIR is not considered accurate if samples present a resistivity below 4,5 Ω.cm for p-type and 0,5 Ω.cm for n-type. Fortunately, no acquired sample had a resistivity below this limit.

The spectroscope used in NorSun was a PIKE technologies map 300 [44]. Through successively measuring the same sample at the same point, the equipment precision was estimated to be 1%, for the standard 64 successive scans. This estimation was considered the best option to find this equipment precision, since it greatly varies with calibration quality, resolution, room atmosphere, forced air flow proprieties and others.

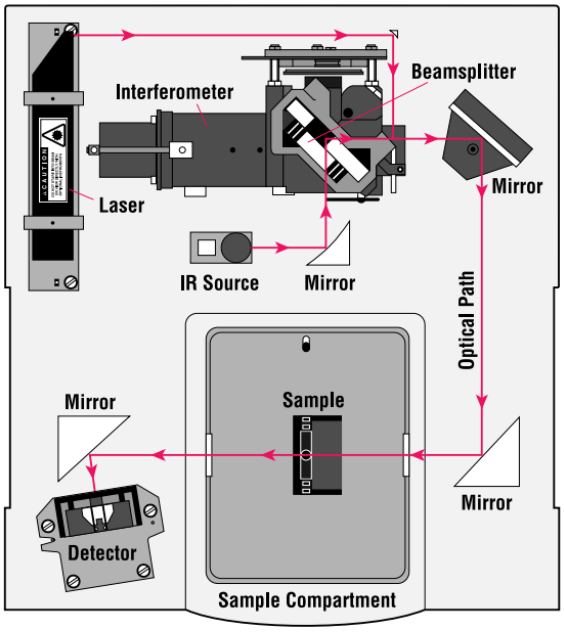

Figure 11: FTIR Spectrometer Schematic [54].
The moving mirror, at the top right corner, allows for a certain range of frequency measures, with a very high resolution. Since the optical path includes a segment that forces the beam to transverse the sample, which is in the room atmosphere, it is important to consider frequent air purging and background checks, for precise measures.

Measurement Procedure

For this study it was necessary to measure several specific variables, such as resistivity, both before and after heat treatment, oxygen concentration and thickness. This last parameter was useful to reduce resistivity measurement errors, as described earlier.

Measuring procedure starts with a simple sample cleaning with ethanol. After drying, which would take no more than a few minutes, the wafer would be positioned in the center of the FPP stage. As standard procedure, each FPP reading consisted in measuring 5 points, one in the center of the sample and 4 other very close to the center (5 mm radius). FPP returned resistivity values for each point, along with an average resistivity value, a standard deviation value and thickness values. All registered thickness values were given by FPP as well. Due to the resistivity dependence of temperature, a temperature sensor was used to certify that the temperature variation between the start and the end of the resistivity measuring would be less than 0,5 ºC.

The samples were then moved to an oven for heat treatment, where they would stay during 17 minutes, in 700ºC. Once accomplished, they would be moved out of the oven and cooled down to room temperature with the help of a forced air flow, slightly colder than room temperature. Once the samples were once again cold enough, they would be once again cleaned and the resistivity measurement would once again be carried out. After this step, FTIR measuring would start.

Before moving the sample to the center of the FTIR stage to measure oxygen content, a background measuring would be performed. This background check is repeated between each sample set (4 to 6 measures). After positioning the wafer in the equipment, FTIR would

measure oxygen and carbon concentration. The scans were repeated 64 times for each sample, as standard procedure. Air purging occurred regularly and it is optimally automated.

Although this was the procedure used for most samples, for some samples the procedure was slightly different. For some sample sets, FTIR would be used both before and after heat treatment, to analyze oxygen and carbon concentration variation with heat treatment. For other sets, oxygen concentration values and resistivity values were retrieved near the samples' borders, to study axial variation. A few other samples, randomly selected, where used to estimate FPP and FTIR mean error.

Position values for every sample were given by NorSun, so no length/position measures were needed.

Measurement Errors

It is important to consider measurement errors, for a better result analysis. In this subchapter, error calculation for each main variable of this study (variation of resistivity, oxygen concentration and position) will be explained.

Position values are accurate to the millimeter unit value. A standard error for distance parameters is usually given by half of the unit precision [49]. Therefore, it was considered that every position value has a flat error of ±0,5 mm. Note that the minimum value for the position of a sample is around 400 millimeters and, therefore, position error does not significantly affect any result.

Resistivity variation error, however, is not as trivial [48]. Due to the lack of specific wafer stage adapter, all wafers were positioned just using the naked eye. It was assumed that this method would have a positioning error of ±5 mm, which will be taken into account with the axial resistivity gradient.

The axial resistivity gradient is the variation of resistivity across the wafer and it is given by the following expression [25]:

$$\nabla\rho = \left(\frac{\rho_r - \rho_{center}}{\rho_{center}}\right)$$

Where ρ_r is the resistivity measured in a certain point other than near center and ρ_{center} is the resistivity measured in the center. ρ_r should preferably be measured at position with half the total radius. This allows for the measured value to be far enough from the center and not close enough to the borders. If resistivity is measured too close to the borders, other corrections factors will be needed.

In the FPP equipment manual it is possible to find a specified precision error of 0,1% precision [40]. During measures, the average derivation has been estimated as 0,75% and, finally, the radial resistivity gradient was estimated to be 8%. Since the variation of resistivity is in fact calculated by subtracting two resistivity values, it is necessary to double the error to retrieve the final total error.

The total variation of resistivity measurement error is, then, calculated by:

$$\Delta\rho errorToT = (Positioning\ error * \nabla\rho + average\ deviation + specified\ precision\ error) * 2$$

Resulting in a value of 2,3%.

oxygen concentration error from FTIR has been estimated to be 0,2 ppm, through successive measuring of the same sample at the same point, for different samples.

9. Modeling

As referred before, oxygen is one of the main impurities contained in CZ-Si and its concentration is requested by CZ-Si industry clients' for quality control. Nowadays, oxygen concentration is mainly measured resorting to FTIR. It is, therefore, interesting to find cheaper and faster alternatives.

The objective of this study is to analyze the close relation between oxygen, thermal donors and resistivity and develop a model that returns the oxygen concentration by inputting variation of resistivity and position values.

The modeling process is usually similar, even between very different areas, and mostly depends on the quality of the data used [50]. A short overview of this process can be easily given assuming three imaginary variables: *x*, *y* and *z*. Also assume that *z* has an unknown relation with *x* and *y*. Therefore, one can also assume that that relation can be expressed by:

$$z = f(x, y)$$

Where *f* is an unknown function. This function can be a very simple linear function or a very complex one, with various degrees and composed by other complex functions. The goal of this numeric modeling process is to find this function *f*, resorting to an adequate data batch of previously measured values for *x*, *y* and *z*. If a model is successful, it will be able to estimate *z* for any given values of *x* and *y*, as long as they still are within a reasonable range.

As referred earlier, there is a close relation between oxygen and thermal donor concentrations and a close relation between thermal donor and resistivity. If one can express thermal donor concentration through temperature, cooling rate and oxygen concentration, than it may be possible to have the following relation:

$$[O_i] = f([TD], T, t)$$

And, since T and t define thermal history, if we assume that, for each position value L along ingot length, for different ingots, the thermal history will be similar enough, the previous expression can be simplified:

$$[O_i] = f([TD], L)$$

On the other hand, it is known that thermal donors have a direct relation with resistivity. Therefore, by measuring resistivity before and after thermal donor dissolution with heat treatment, that resistivity variation will express the thermal donor concentration and, finally:

$$[O_i] = f(\Delta\rho, L)$$

Resistivity measurement is a much simpler, cheaper and faster procedure than direct oxygen concentration measurement through FTIR. Therefore, if a model has enough accuracy, it may be an interesting alternative for quality control procedures.

To find *f*, one may resort to a method referred as curve fitting. This method implies the creation of the function that better fits the points of the measured data batch. The models' creation and optimization methods will be described during the following paragraphs.

Curve fitting

Curve fitting method implies the creation of a function that better fits a certain series, using one or more series of variables and integers, usually found through iteration. If the samples used are adequate, this function used for curve fitting may be used to estimate values within a reasonable range [52].

Usually, polynomial functions may express a good curve fitting, if applying the right integers. Integers can be optimized through least squares method, described during the next subchapter. A general expression for a second degree polynomial with two variables may be:

$$z = \beta_0 + \beta_1 x + \beta_2 y + \beta_3 xy + \beta_4 x^2 + \beta_5 y^2$$

Where β are the integers, z the estimated value, x and y are the variables of the predictive function. For this study, a direct translation of this expression would be:

$$[Oi] = \beta_0 + \beta_1 L + \beta_2 \Delta\rho + \beta_3 L\Delta\rho + \beta_4 L^2 + \beta_5 \Delta\rho^2$$

Where L refers to position along the length of the CZ-Si, $\Delta\rho$ is the variation of resistivity between before and after heat treatment and $[O_i]$ is the concentration of oxygen, which it is meant to be predicted. This topic will be explained deeply during the next chapter.

Although this is a simple expression, functions resulting from curve fitting may be rather complex. Integers result in degrees of freedom and a higher number of degrees of freedom may lead to a better curve fitting. Nonetheless, it is important that the integers are related with the variables. A combination of different functions may help in the curve fitting process if the variables have a complex relation. The following general expressions were tested, in combination with polynomial equations from first to forth degree and in combination between themselves.

Rational function: $z = \beta_{0+} \frac{\beta_1}{x} + \frac{\beta_2}{y} + \frac{\beta_3}{xy}$

Exponential function: $z = \beta_0 + \beta_1 e^x + \beta_2 e^y + \beta_3 e^{xy}$

Logarithmic function: $z = \beta_0 + \beta_1 \ln x + \beta_2 \ln \beta y + \beta_3 \ln xy$

Trigonometric function: $z = \beta_0 + \beta_1 \sin x + \beta_2 \sin y + \beta_3 \sin xy$

Polynomial with undefined degrees: $z = \beta_0 + \beta_1 x^{\beta_2} + \beta_3 y^{\beta_4} + \beta_5 (xy)^{\beta_6}$

Although these combinations may reach a very large number of parameters (above 50), the optimization of the integers will delete the parameters which show no relation with the

measured data series that the model is supposed to predict. The optimization of the model through the analysis of the model's performance characterizers may successfully return a function with high prediction accuracy.

Least Squares and average error

Least Squares method is one of the main steps for the data fitting process. Having a series of measured and estimated values, it is possible to create the respective residual series [51]. A residual is the difference between a measured value and the respective estimated value, indicating the how accurate is the predictive function. For this study, a residual value is given by the following equation:

$$[O_i]Residual = [O_i]estimated - [O_i]measured$$

To analyze a whole data set, it is necessary to consider the residuals for every point of analyzed data. Since that, there are, usually, both negative and positive residuals, a simple sum of all residuals will not suffice. Least squares method uses a parameter referred as the sum of the square differences (*SSQdif*), given by:

$$SSQdif = \sum([O_i]estimated - [O_i]measured)^2$$

When this sum is a minimum, the value of the residuals is as close of zero as possible, which means that the curve fitting is at its optimum. Therefore, it is possible to change the function integers' iteratively in order to find this minimal value, i.e., the value of the integers of the predictive model that fit the measured curve the better.

This method, besides allowing the integers' optimization, also allows a direct comparison between different models, for the same data set. Sometimes it is important to compare the model performance between different data sets. If a data set has a higher number of measured values, i.e., the data set is larger, it may result in a higher value for the *SSQdif*, even if the model performs better. To a better model comparison, it was used an average error value:

$$AvgError(\%) = \overline{\left(\frac{\sqrt[2]{([O_i]measured - [O_i]estimated)^2}}{[O_i]measured}\right)} * 100$$

Or one can express the model precision:

$$Model\ precision(\%) = 100 - AvgError(\%)$$

These parameters allow a good understanding of the overall model performance, independently of the size of the data fitting. It is, nonetheless, important to understand that if a model is able to successfully fit a larger data set, it means it is more successful. On the other hand, if a model is created based on a small data set, curve fitting results may be misleading.

Models

Models were created using Microsoft Excel program. R statistics program was also tested to the same purpose but with slightly worse results.

Each point has a value of position, variation of resistivity and measured oxygen associated. A created equation, with random values for the integers, would be applied to each point of the data series, having variation of resistivity and position as variables. Through least squares method, the value for the sum of the square differences would be found. The optimization of the integers was achieved using Solver Add-in of Microsoft Excel, which would automatically find the integers which minimize the sum of the square differences [53]. The Solver Add-in would be rerun as many times as needed for the integers to have an optimal fixed value (usually two or three runs would suffice).

This process was repeated until it was considered that the curve fitting process had already fit the data set close to optimally (roughly 40 different equations were tested). This point will be addressed deeply during the discussion.

Two different models were created. The first one, which will be from now on referred as base model, was built to optimally fit the complete data set, regardless of the position.

The second model, however, is in fact a combination of 5 different models, one for each position range. As referred before, all the data acquired had the particularity that it is divided in 5 different very short position ranges. This is because all the samples measured were from the tail of cut blocks, which have a very fixed defined position for all ingots. This model will, during discussion, be referred as model TX (TailX) as X being the block number from where the sample was cut. As an example, the modelT1 is related to all the samples from the first block.

Different tests were run for different data sets. The purpose of these tests will be described during the next chapter.

Additionally, a simulation of the crystal growth has been run through SGSim, using the solid fractions of the ingot 2718A as representative of the average crystal growth pattern, as to better understand the thermal donor formation relation with the cooling rate.

10. Results

The following chapter will present the data acquired during this study. This will not only include data from sample measurements, but also the different model results.

Radial oxygen Variation

As referred before, for the first set of samples, the oxygen concentration was measured both in the center and near the borders of the samples. The following graphics present the concentration of oxygen along the length of the ingot. The values taken near the borders are, in fact, the average value of 4 points, measured near each corner of the wafer. The value difference of those points, for the same sample, is almost negligible.

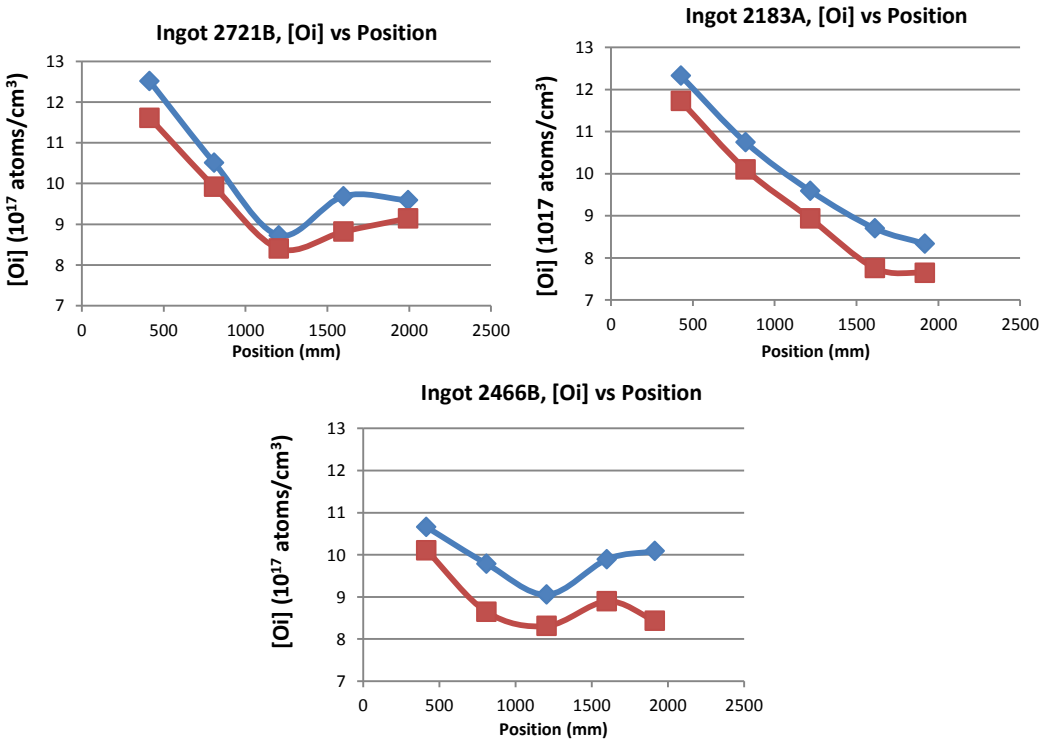

Figures 12; 13; 14: Oxygen concentration (center and borders) versus Position.
Blue lines stand for oxygen measured in the center, red lines stand for the average oxygen measured near the borders of the wafers.

Oxygen and Resistivity Axial Variation

The following figure presents the oxygen concentration and resistivity variation along the ingots for the second set of samples, composed by 6 ingots. The main purpose of this graphic is to recognize the different general curve patterns and the relation between the oxygen concentration and the resistivity variation.

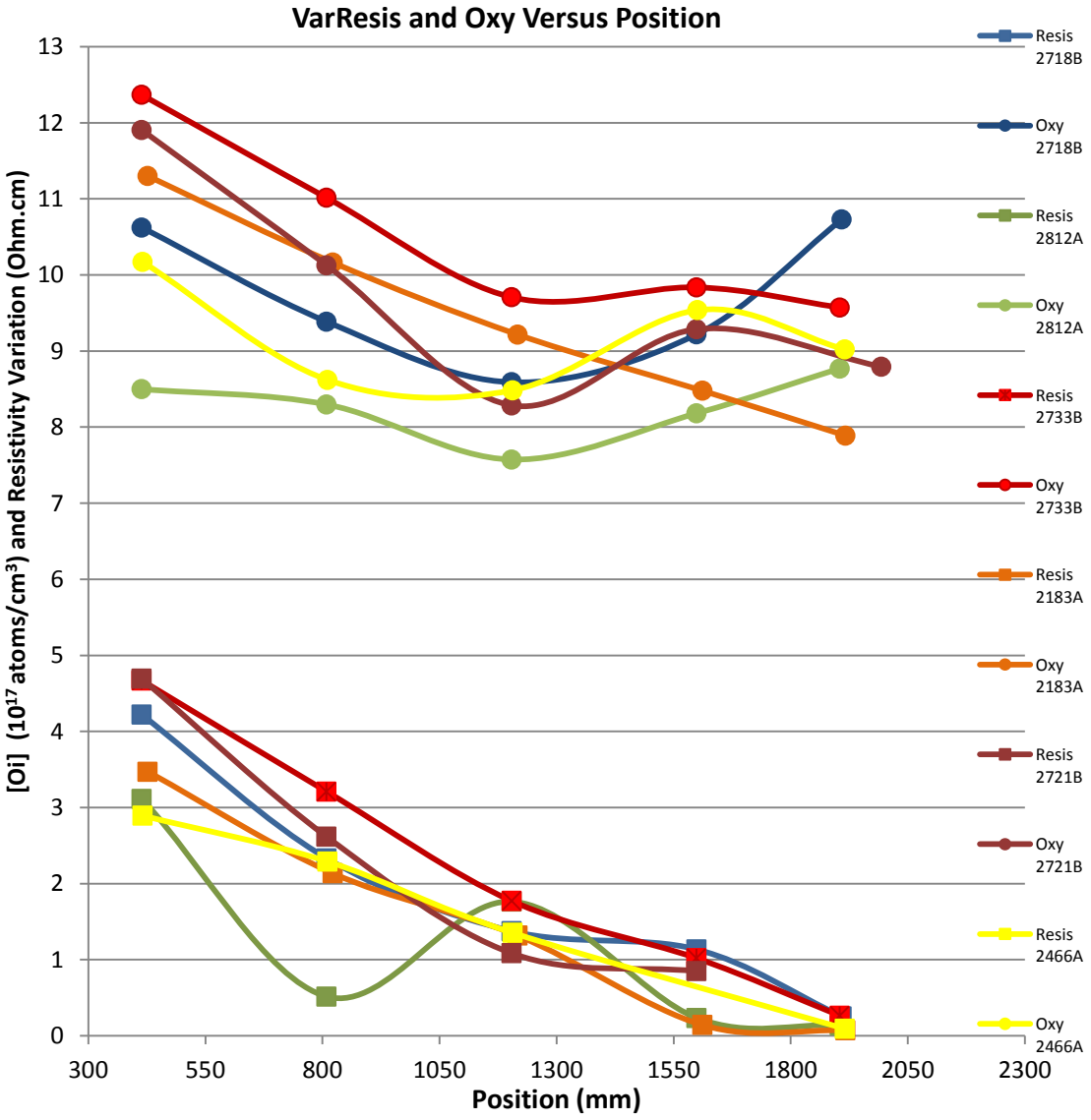

Figure 15: Oxygen and resistivity variation VS position.
Each color represents a specific ingot, circles represent oxygen concentration and squares represent resistivity variation

Oxygen concentration BHT and AHT

The following figures represent the oxygen concentration along the ingot, both before and after heat treatment, for 6 different ingots. The red lines stand for oxygen concentration after heat treatment and blue lines stand for before heat treatment.

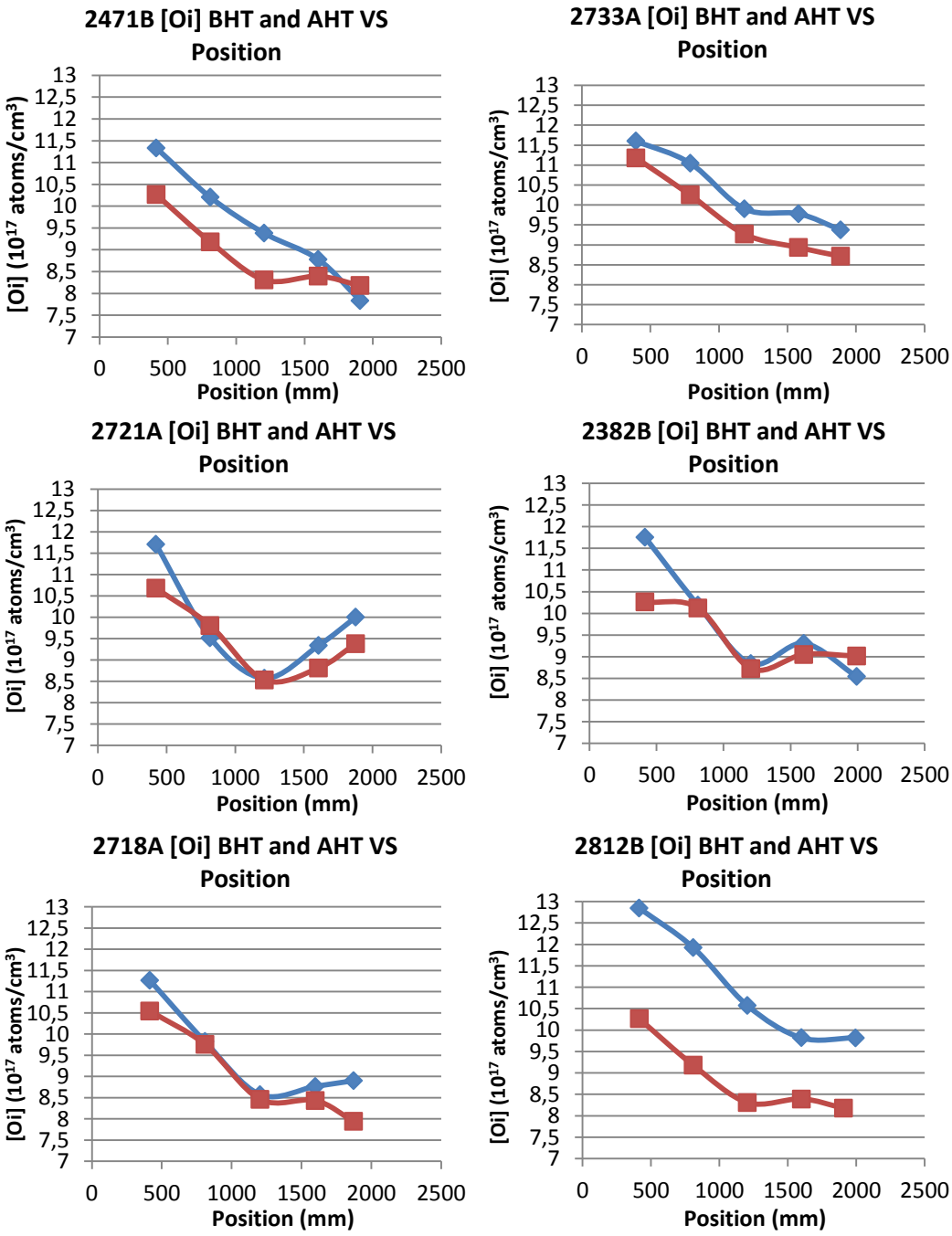

Figures 16; 17; 18; 19; 20; 21: oxygen concentration BHT and AHT versus position.
Red lines stand for oxygen AHT and blue lines stand for oxygen after heat treatment.

Oxygen and Resistivity Variation for fixed position

As explained earlier in this work, all samples measured belong to one of five different position sections, with fairly short ranges for each section. Thus, it is possible to fix the position parameter and plot oxygen concentration versus resistivity variation. The following charts express such values, for each TX section. These charts include the complete sample set.

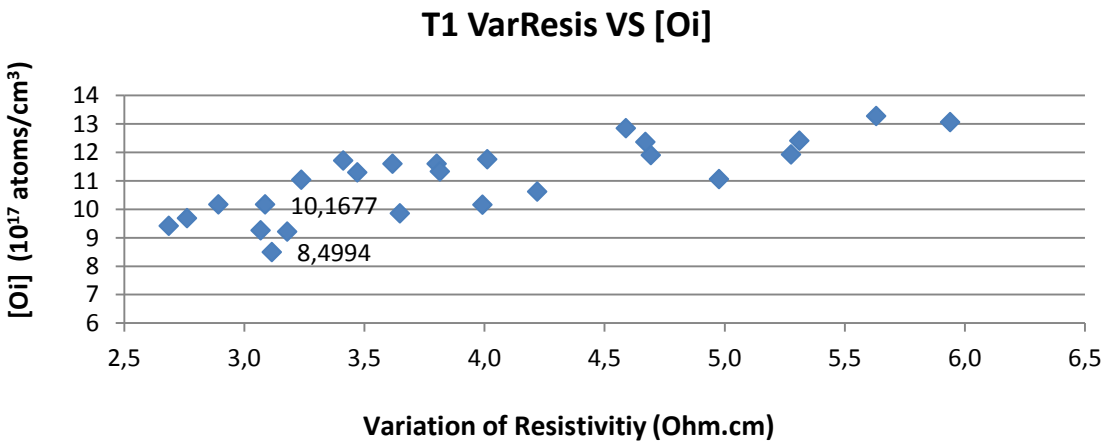

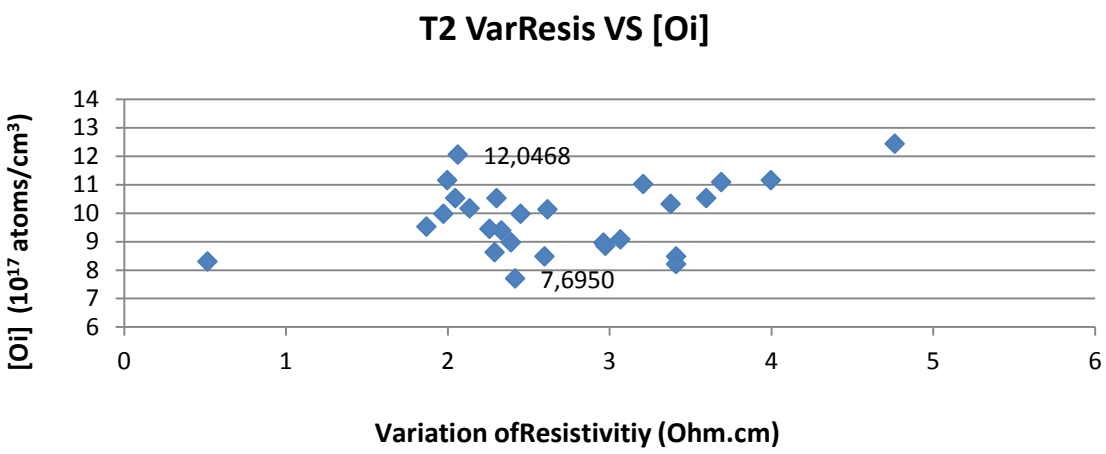

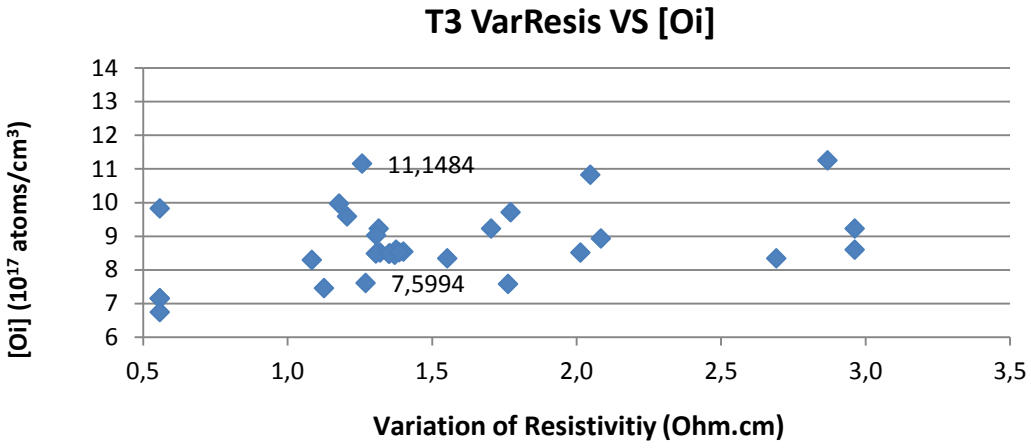

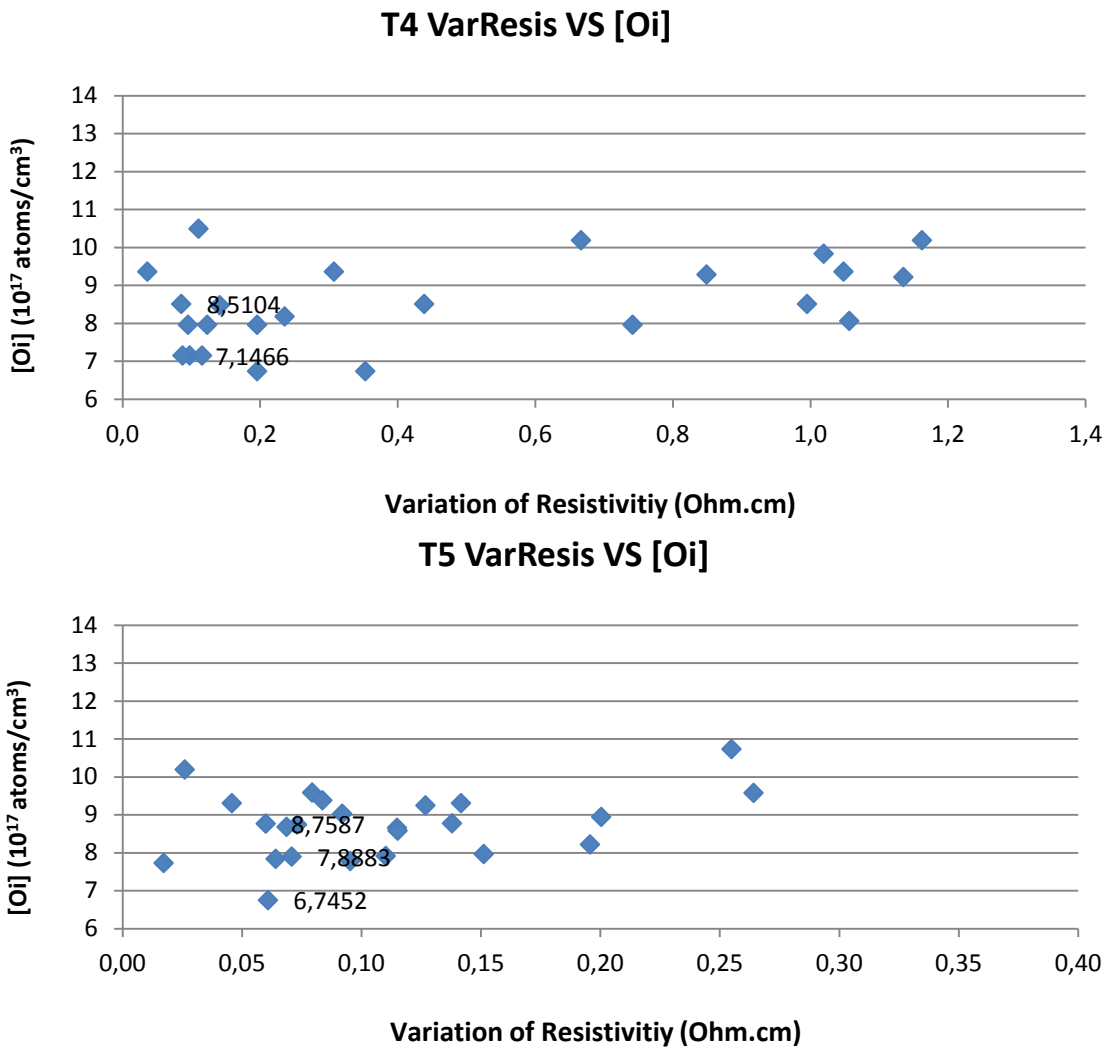

Figures 22; 23; 24; 25; 26: oxygen concentration versus variation of resistivity.
The amplitude values for the positions ranges T1, T2, T3 and T4 are 40mm. T5 presents an amplitude value of 122 mm.

Base Model Results

The following charts present the results of the created model, assuming the same algorithm for all the samples, without regard to the position group. Red colors stand for predicted oxygen values and blue colors stand for the measured values. The complete results for this model and all other model applications can be found in the attachments of this work.

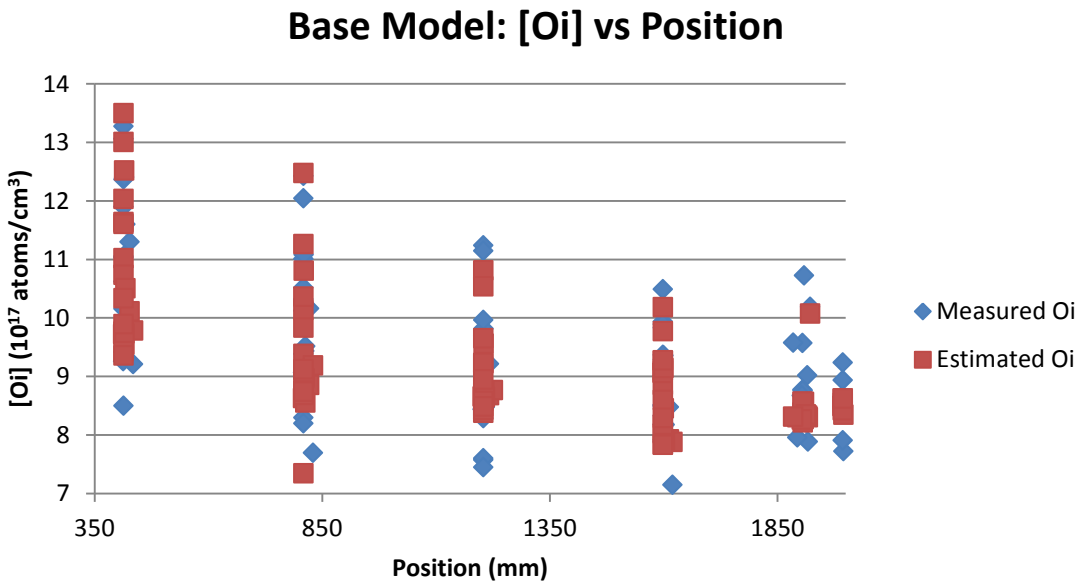

Figure 27: Base model results for oxygen concentration predictions along the ingot. Note the clear position groups.

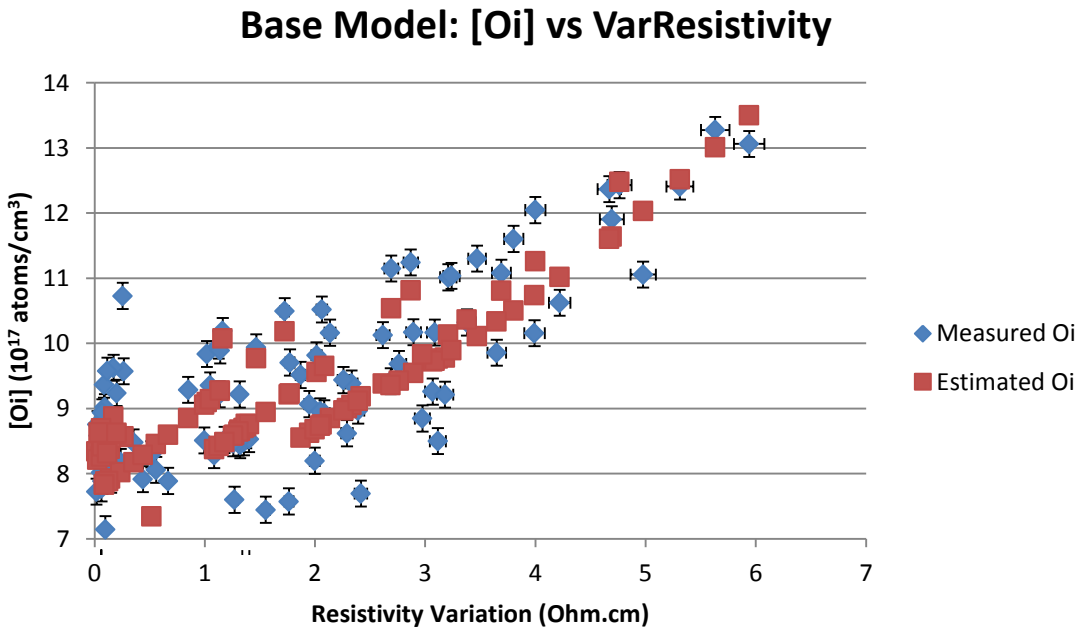

Figure 28: Base model results for oxygen concentration predictions, in function of variation of resistivity.

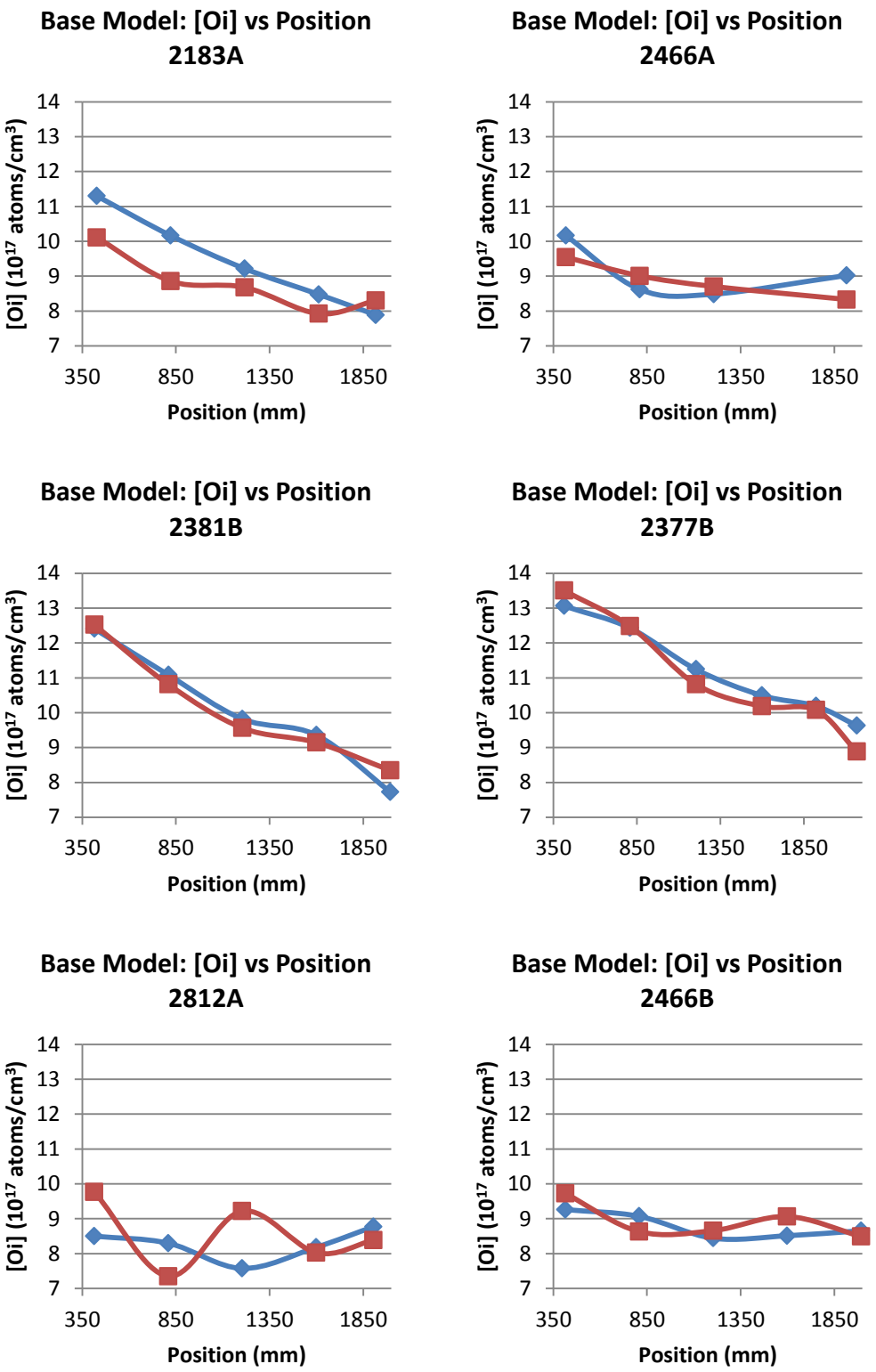

Figures 29, 30, 31, 32, 33, 34: Examples of the base model application in specific ingots. The first pair of examples show an average correlation, the second pair a good correlation and the third pair a bad correlation. Blue lines represent measured values and red lines represent estimated values.

TX Model Results

The following charts present the results of the created model which algorithm is optimized and independent for each position group. Red colors stand for predicted oxygen values and blue colors stand for the measured values.

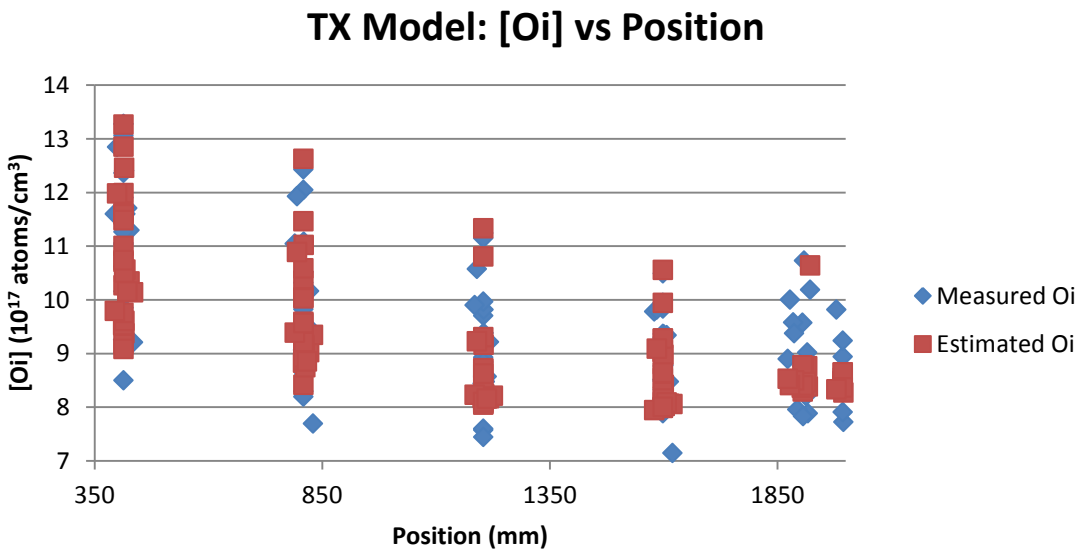

Figure 35: TX model results for oxygen concentration predictions along the ingot.

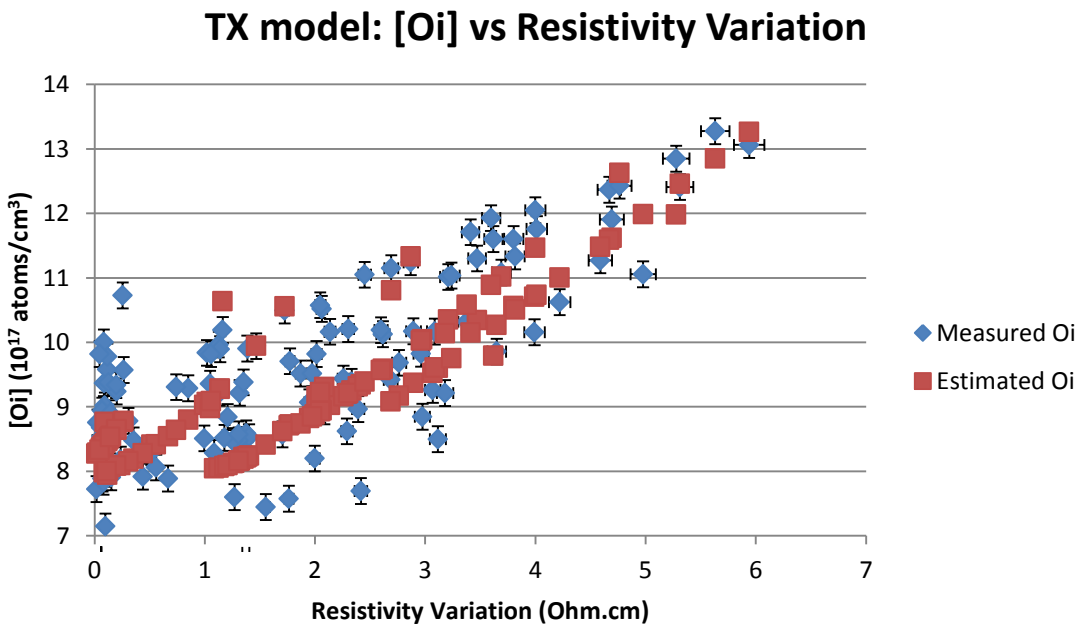

Figure 36: TX model results for oxygen concentration predictions, in function of variation of resistivity.

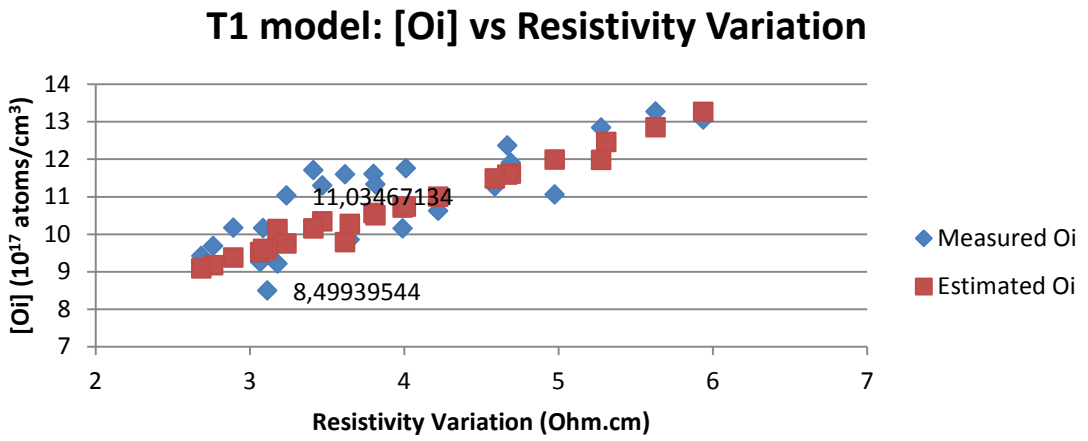

Figure 37: TX model results for oxygen concentration predictions, in function of variation of resistivity, first position group

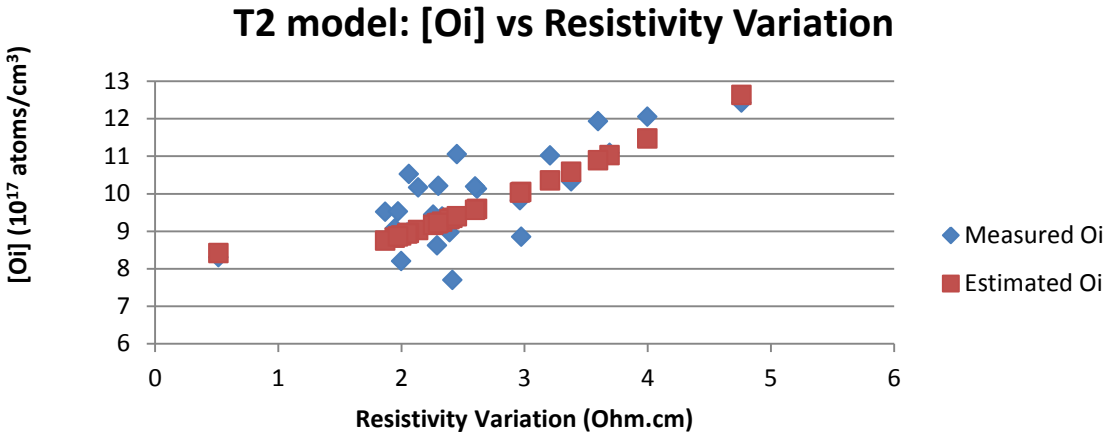

Figure 38: TX model results for oxygen concentration predictions, in function of variation of resistivity, second position group.

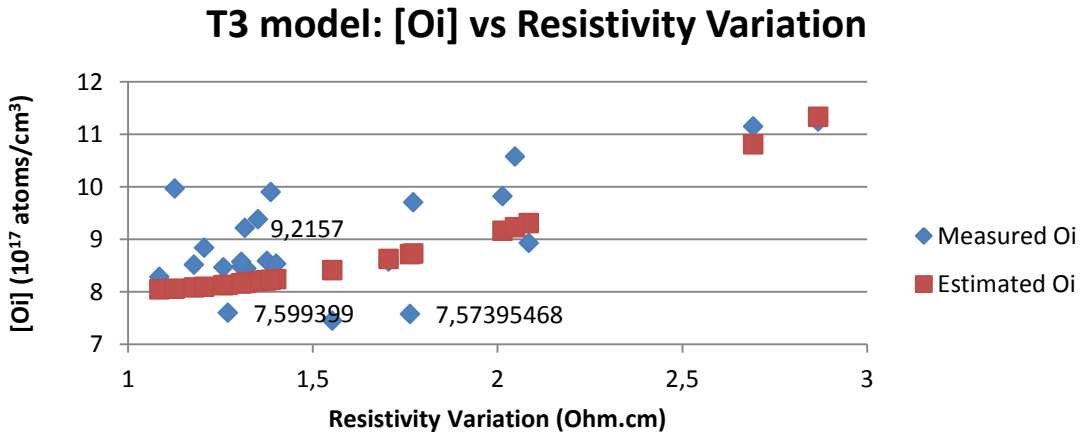

Figure 39: TX model results for oxygen concentration predictions, in function of variation of resistivity, third position group.

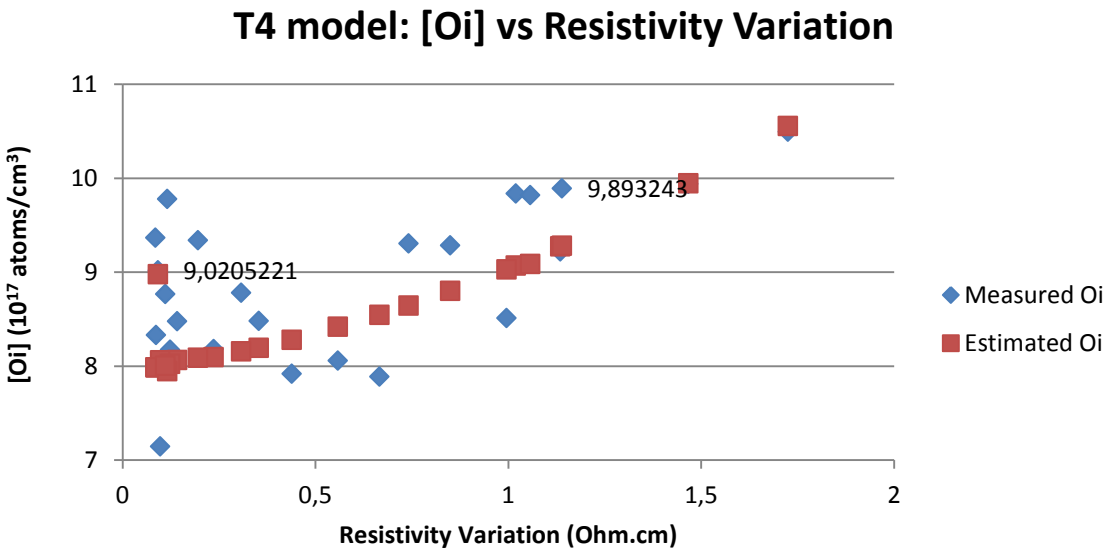

Figure 40: TX model results for oxygen concentration predictions, in function of variation of resistivity, forth position group.

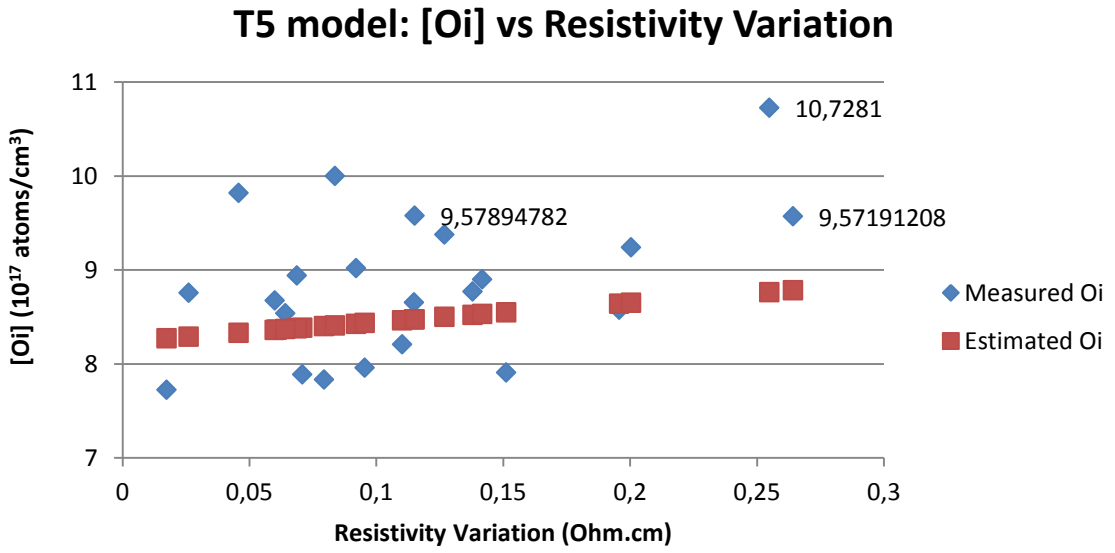

Figure 41: TX model results for oxygen concentration predictions, in function of variation of resistivity, fifth position group.

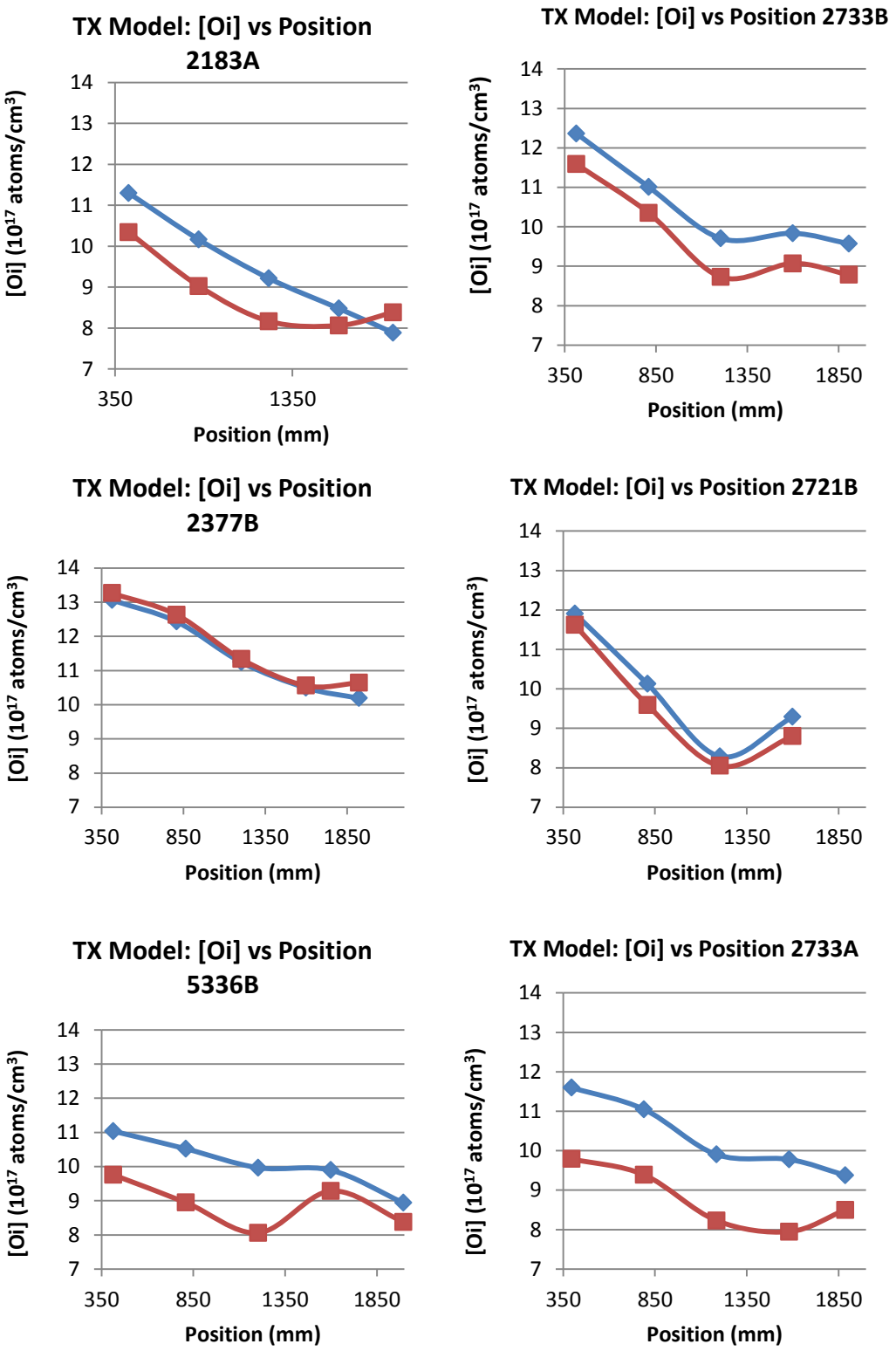

Figures 42, 43, 44, 45, 46, 47: Examples of the TX model application in specific ingots. The first pair of examples show an average correlation, the second pair a good correlation and the third pair a bad correlation. Blue lines represent measured values and red lines represent estimated values.

TX model results: Filtered sample set

The TX model has been applied to a smaller sample set, namely the best 15 ingots out of a total of 25 ingots. Red colors represent predicted values and blue colors represent measured values.

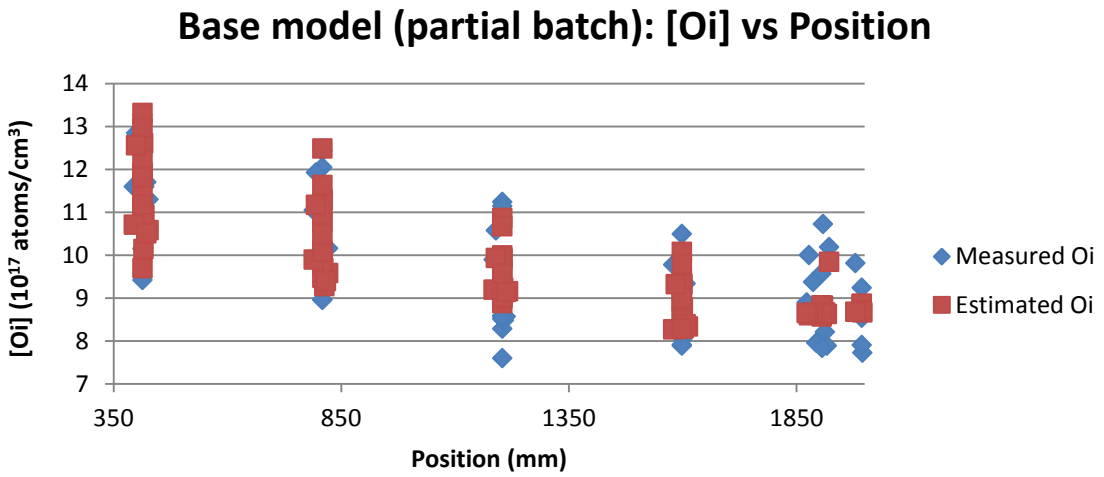

Figure 48: Base model results for oxygen concentration predictions along the ingot, applied for partial batch.

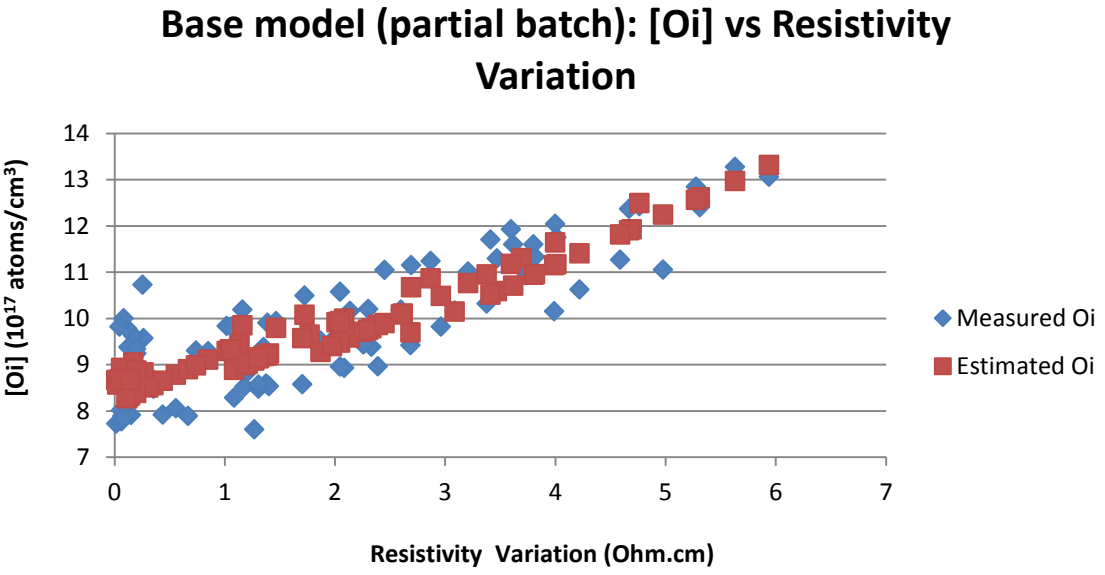

Figure 49: Base model results for oxygen concentration predictions, in function of variation of resistivity, applied for partial batch

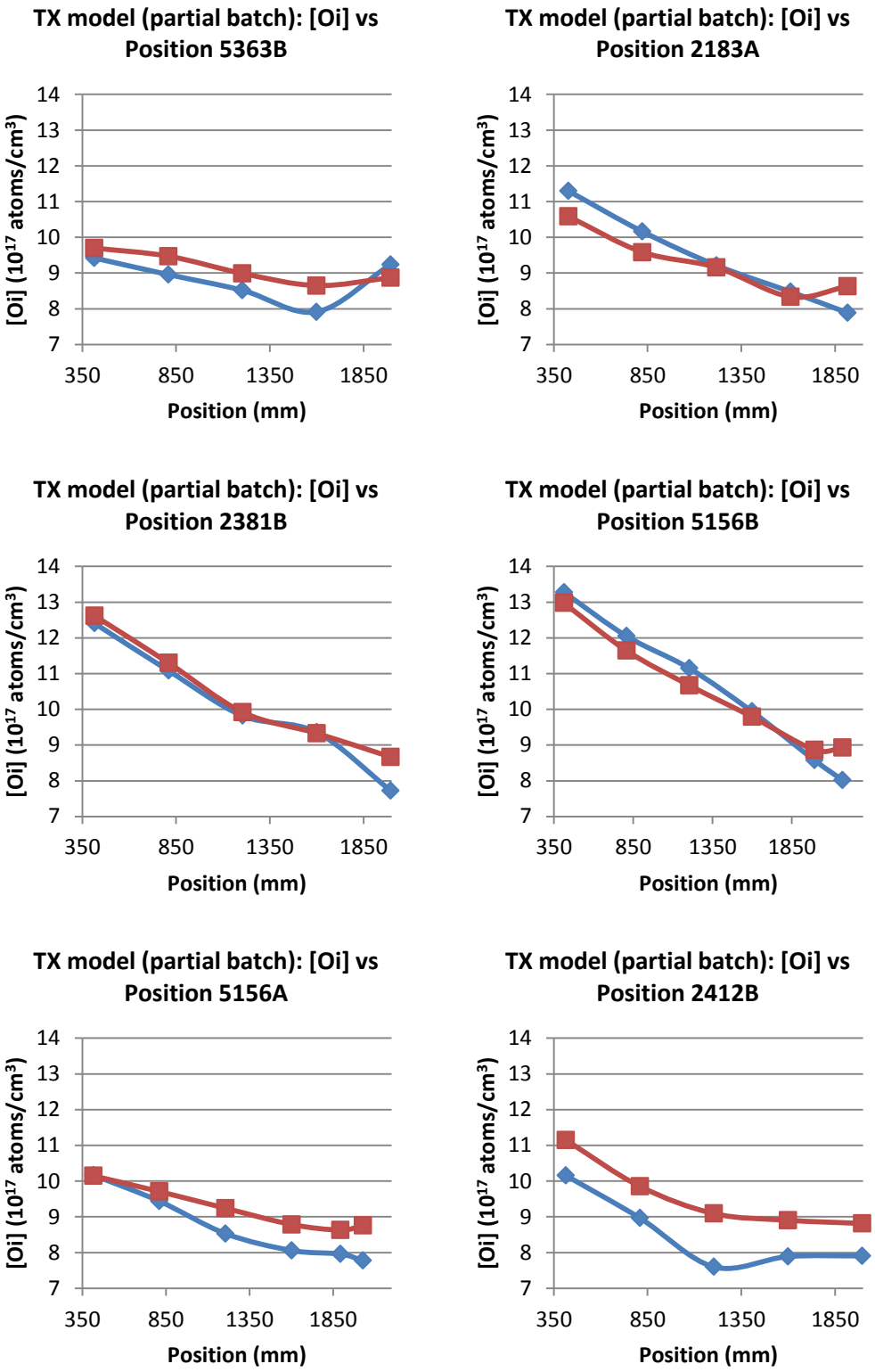

Figures 50, 51, 52, 53, 54, 55: Examples of the TX model application in specific ingots, for a partial batch. The first pair of examples show an average correlation, the second pair a good correlation and the third pair a bad correlation. Blue lines represent measured values and red lines represent estimated values.

Model Results: [Oi] BHT vs [Oi] AHT

The oxygen concentration of 6 ingots, each with 5 different test wafers, has been measured using the FTIR equipment, both before and after heat treatment, with the purpose of comparing the model's performance for each set of measures. The following charts represent the model results. Red colors stand for predicted values and blue colors stand for measured values. For a best direct comparison, each pair of charts, which represent the results using, respectively, oxygen concentration values before heat treatment (left side) and after heat treatment (right side), will be placed side by side, for each ingot.

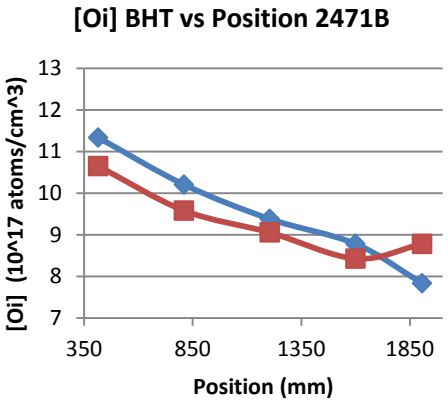

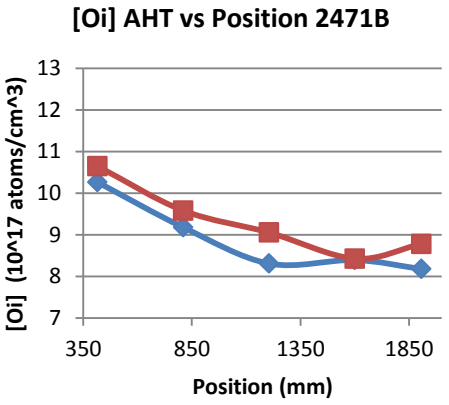

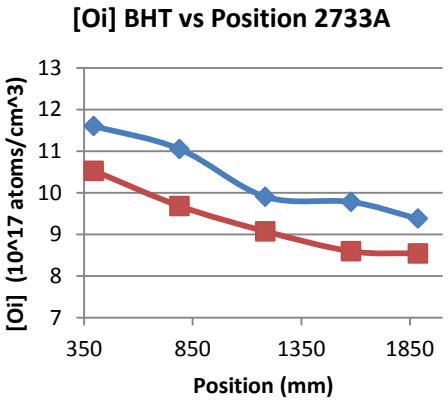

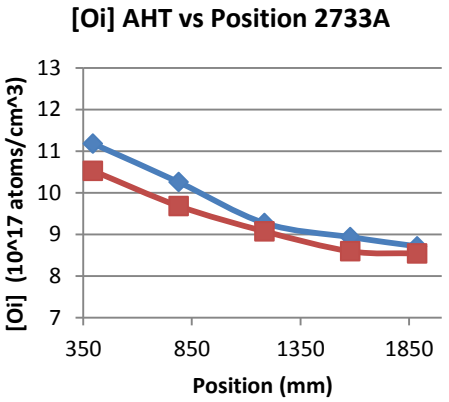

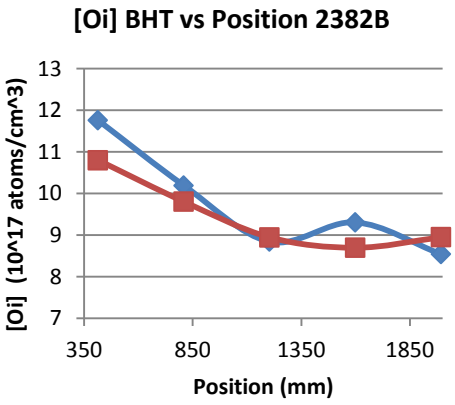

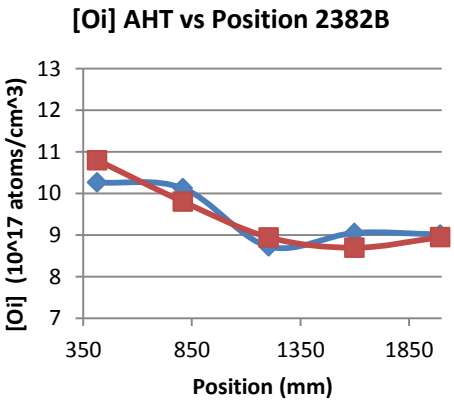

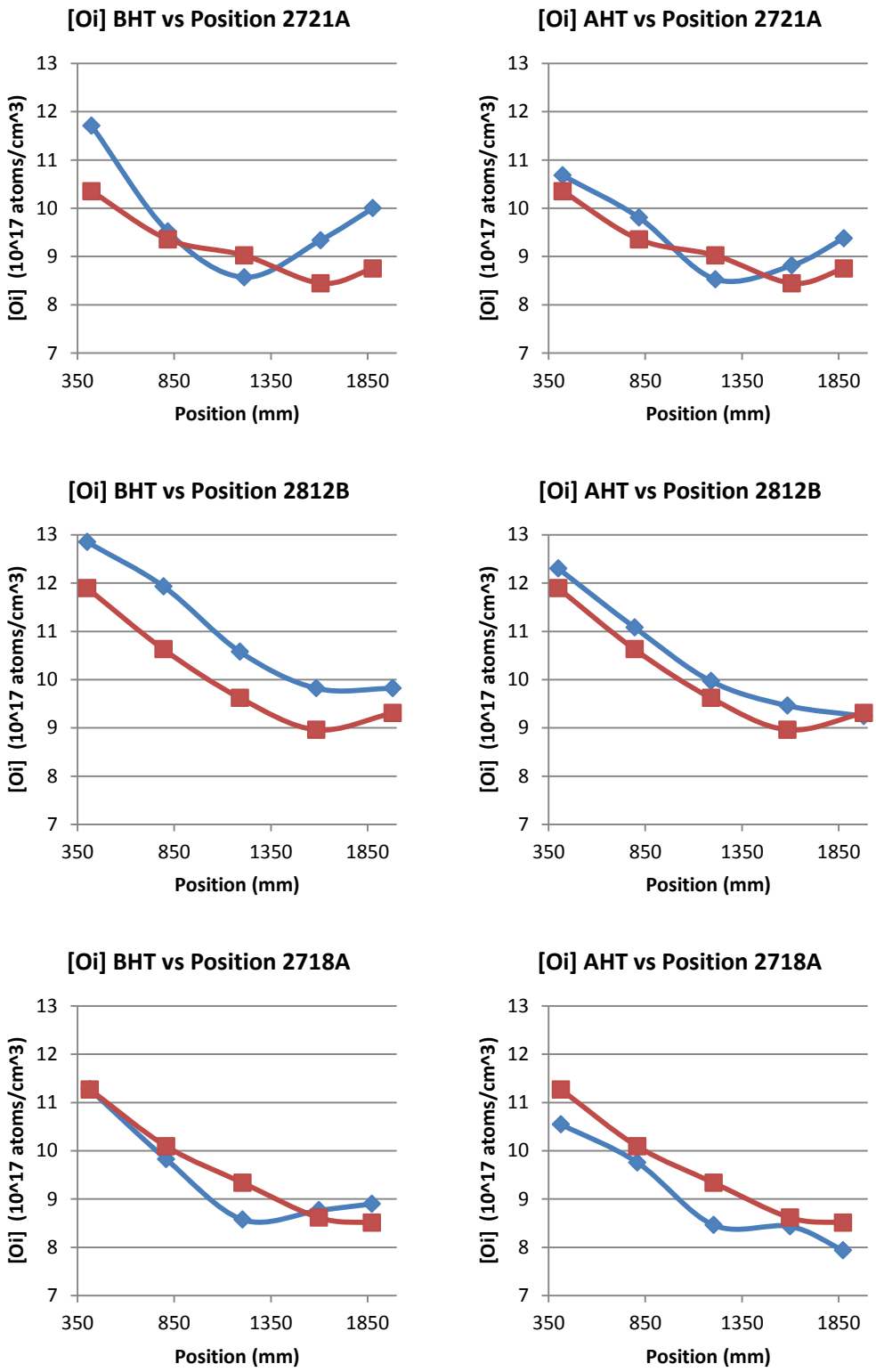

Figure 56, 57, 58, 59, 60, 61, 62, 63, 64, 65, 66, 67: Ingots characterized to compare model results using either before heat treatment (BHT) or after heat treatment (AHT) oxygen concentration measures. Red lines represent predicted values and blue lines represent measured values.

Heat treatment performance analysis

Two samples from the same ingot, from position T1 and T5 respectively, were cut in half as one pair was heat treated in NorSun and the other pair has been heat treated in NTNU. The following table presents the results of the measures taken for such samples.

Ingot	varρ	var [Oi]
T1 NorSun	2,7537	-0,3286
T5 NorSun	0,1085	-0,3146
T1 NTNU	1,6254	-0,1991
T5 NTNU	0,1325	-0,1801

Table 1: Heat treatment performance analysis results. T1 are the samples close to the seed and T5 are the samples close to the tail.

Simulation Results

A simulation of the crystal growth has been run through SGSim, using the solid fractions of the ingot 2718A. The following table and chart present the results of the simulation, along with the respective resistivity variation and oxygen concentration values. Temperatures are presented in Celsius. Tcenter stands for the estimated temperature in the center of the crystal and Tedge stands for the estimated temperature at 5 mm from the edge.

Position	varρ	[Oi]	Tcenter	Tedge
395	4,5895	11,2701	1411	1411
790	2,9625	9,8237	617	611
1185	1,7050	8,5739	-	-
1580	0,1107	8,7671	244	243
1854	0,1418	8,9006	190	189

Table 2: Crystal growth simulation results.

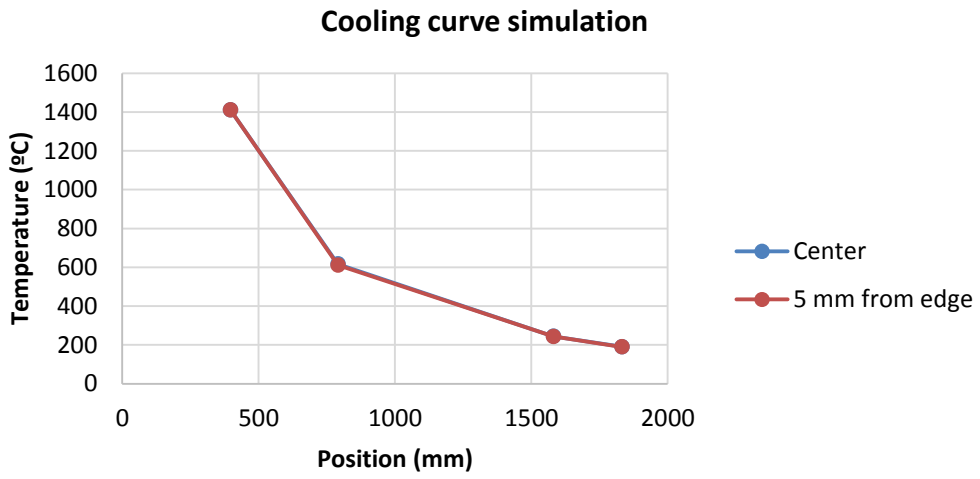

Figure 68: Cooling curve drawn from the simulation results.

11. Discussion/Analysis

In this chapter, the results obtained and described Chapter 10 will be analyzed and discussed. Each topic will be addressed in the same order as presented in the previous chapter, for an easier understanding.

The results acquired for the oxygen concentration radial variation (Figures 12, 13 and 14) shown an expected behavior. As explained earlier in this work, the oxygen concentration is slightly higher in the center of the ingot due to how the oxygen is incorporated in the crystal and what mechanisms are used to reduce this issue, namely forced air flow and crucible/crystal rotation. Averagely the oxygen concentration at the edge is 10% lower than in the center, which is within the normal range of values.

An overall understanding of how the resistivity variation with heat treatment, as well the oxygen concentration, changes along the ingot, is possible by analyzing Figure 15. The resistivity variation presents, for most cases, an almost linear decrease along the ingot. This is expected since it is known that the concentration of thermal donors, which is what directly affects the resistivity variation, also decreases along the ingot. Oxygen concentration shows a similar behavior, until the middle section of these ingots, again with an almost linear decrease of its value. Starting from the middle section to the tail wafer, it is possible to notice three different patterns. One of the patterns is a simple linear decrease of the oxygen concentration. This behavior can be easily verified with the 2183A (orange) wafer samples. Another different pattern is a continuous increase of the oxygen concentration along the ingot, just like the 2718B (blue) samples. A final different pattern can be recognized when analyzing the 2466A samples (yellow), with a very clear oxygen concentration increase, followed by subsequent decrease. The understanding of the overall curve patterns is important for both model formulation and post-analysis, due to the number of freedom degrees that needs to be considered.

From Figures 16 to 21, it is possible to understand that the oxygen concentration usually decreases with heat treatment, which may be explained by a re-precipitation of the oxygen during cooling. This phenomenon was the motivation to study the performance of the heat treatment procedure in NorSun, through comparison with the heat treatment procedure in NTNU. One can also notice that, for some samples, such as 2718A, the heat treatment did not result in a high variation in the oxygen content but, for some other cases, such as 2812B, the difference of oxygen content before and after heat treatment is extremely relevant.

One of the assumptions of the theory that supports the creation of the model, that this thesis studied, is that the oxygen concentration can be given by a function of variation of resistivity and position. This assumption is only met if the thermal histories of the ingots, from which the sample set was acquired, are similar. If not, a model will not be able to accurately predict the wanted parameter. Knowing this, if several samples, for the same value of position, present a very different value of oxygen concentration for the same value of variation of resistivity, it may be an indicator that the sample sets do not meet the requirements. In fact, analyzing Figures 22 to 26, it is possible to notice that certain samples rectify this point. For T1 and T2, considering that some samples are, in fact, outliers, one can notice a pattern. Unfortunately, for end position samples, the dispersion of values increases, which have a direct effect in the precision of the created model.

The base model was applied to the complete data set, returning a precision of 93,87% and a maximum error of 30,13%. Although the point which leads to such an high error may seem like an outlier, some other points also show a deviation from the measured result that reaches the 25%, which may indicate that the model, although it has a fairly good precision, it does not always respects the curve trend.

By analyzing Figure 27, we can easily distinguish each of the five different position groups from each sample belongs to. It is also easy to recognize a clear decrease of the amplitude of the oxygen concentration values along the ingot, indicating that, during the solidification process, the oxygen incorporation in the crystal is progressively stabilizing. Figure 28 gives a better understanding of the model performance and how the measured values are scattered. Note the number of points allocated at low resistivity variation values. These points belong at the end positions of the ingot, where the thermal donor concentration is much lower due to the particularities of the thermal history in such positions. Such low values may interfere with the model precision quality. Nonetheless, a better understanding of the mode performance can be achieved by studying the results of isolated ingots, as Figures 29 to 34 present. As described in the caption, the first pair of figures show results of average quality, the second pair show good model performances and the third pair show examples of a bad performance. Although the predicted curves have an acceptable fit to the measured points, the worse results are justified by the inability of the model to respect the results trend. This is in fact expected, as the model is being applied to the complete batch and, as shown by Figures 22 to 26, many points could not be respected by a single function simultaneously.

The TX model does not show a much better precision compared with the base model, with a value of 93,93%. On the other hand, the maximum error shown a value of 24%, which may lead to the conclusion that this model can fit more uncommon trends. In fact, this is unexpected since this model has a much higher flexibility during the curve fitting process, due to a different algorithm applied to each position group, against a single algorithm for the whole data set as in the base model.

It is not simple to compare the overall charts for this model (Figure 35 and Figure 36) with the corresponding charts of the base model, as almost to no difference can be found. Nonetheless, it is interesting to compare the model results with the measured oxygen values in function of the resistivity variation, already presented in Figures 22 to 26. As already mentioned, the difference between the lowest and highest position value for each group is only 4 centimeters, with the exception of the fifth group, with a maximum difference of 10 centimeters. As the body length of each ingots reaches 2 meters, it is viable to consider that, for each position group, this variable has no major influence in the oxygen concentration values. By analyzing Figure 37, which corresponds to the first group, we can see that the measured values have a clear trend, with the oxygen concentration increasing along increasing resistivity variation values. This trend is not so clear but also exists along other different groups, which is, again, not unexpected, as a higher resistivity variation corresponds to a higher thermal donor concentration and it is known that a higher oxygen concentration also leads to higher thermal donor concentration. Nonetheless, the measured values scatter in such a way that it is not possible for an algorithm to fit all data even within the same position group. A few isolated points were marked in the charts, with the explicit oxygen concentration value. These values are either aligned vertically, with very different oxygen concentration values but with very similar resistivity variation values, or aligned horizontally, with very similar oxygen concentration values for very different resistivity variation values. As we move along the ingot to different position groups, oxygen

values almost appear randomly scattered. The last position group, in Figure 41, we find almost no correlation between the estimated values and the measured ones, as the model assumes a linear trend with very similar values for every sample. There is the chance that the position of these samples is fixed enough, as its 6 centimeters higher than the previous groups, but most likely the lack of model adjustment to the measured values is due to the very low resistivity variation values. Since, for the end positions of the ingots, the thermal donor concentration is actually very low, due to the thermal history characteristics (namely fast cooling rate), it is not possible to apply this model correctly.

Again, 6 examples of this model for specific ingots are presents (Figures 42 to 47) and, again, the first pair presents average results, the second pair good results and, lastly, a pair with bad results. The first thing one may notice is that the overall trends are much more respected than the previous model. As referred above, this is due a much higher flexibility of the model. Nonetheless, it is possible to notice some difference between the predicted values and the measured values which is mainly due to the vertical aligned points presented in the previous charts, as the model tries to create a curve that fits all samples of the same position.

The TX model, applied for a partial batch of the best 15 ingots out of the 25, shown a precision of 95,03%, with a maximum error of 15,87%. This improvement is mainly related to the reduction of the sample set tested, as the samples with worse results are not included. This leads to a considerable better curve fitting process, as well as a better approximation of the predicted oxygen value to the real one. Again, from Figure 49, one can see that the relation with the model results with the measured values is still low for very low values of resistivity variation. By analyzing Figures 50 to 55, we can see a much better curve fitting, even for the worst results. The vertical curve positioning is also better, compared with the previous results.

As mentioned above, the high oxygen variation of the test wafers when submitted to NorSun's heat treatment was not expected. As so, 35 samples, which were directly retrieved from 6 ingots, were selected and, for those samples, the oxygen concentration would be measured both before and after the heat treatment. The model was applied for both set of results, as shown by the Figure 56 to 67. After all optimization processes, the curve fitting returned a precision of 94,47%, with a maximum error of 16,4% for before heat treatment measures set and, for after heat treatment, a precision of 95,64% and a maximum error of 10,35%. It is worth noting that the model function optimization for these two specific tests only take in account those 35 samples, as these results are completely independent of previous results. Against what is expected, but according NorSun's standard quality control procedure, it seems that this oxygen variation with the heat treatment actually leads to slightly better results. Nonetheless, as the number of samples is actually rather small, it is wiser to assume that the oxygen variation with this heat treatment is simply not relevant to affect the model's performance.

As for the results taken from the heat treatment procedure comparison between NTNU and NorSun (**Error! Reference source not found.**), there are also a few interesting and unexpected points to comment. Firstly, it is important to note that samples near the tail, denominated as the T5 samples, have a very low concentration of thermal donor, which will lead to a very low resistivity variation, independently of the heat treatment, as the results prove. Nonetheless, it is still possible to compare the variation of oxygen, which is considerably higher for the NorSun's heat treatment. This negative variation of oxygen may lead to the formation of oxygen complexes that may alter the crystal lattice proprieties and reduce wafer quality. One the other hand, the resistivity variation for the T1 sample treated in NorSun is much higher when

compared with the sample treated in NTNU. As a higher resistivity variation directly translates to a higher concentration of destroyed thermal donors for the same sample, one can conclude that NorSun's heat treatment may be more effective than NTNU's at thermal donor killing. Still, just one sample may not be enough to justify the results.

Finally, the crystal growth simulation is to be addressed. The ingot 2718A has been selected to be representative of the average crystal growth pattern. The temperature for four positions has been estimated, for two different points, namely a point located at the center of the ingot and a second point at 5 mm from the edge of the crystal (**Error! Reference source not found.**). First, one may notice the temperature similarities between the center and the edge, for the same position, which differences are almost unnoticeable in the Figure 68. This is due to a slow crystal growth (assumed as a constant 1 mm/min), which leads to this low radial thermal variation. This is fortunate, as a higher radial thermal variation would lead to thermally induced stresses, resulting in structures losses. As the crystal growth is assumed to be constant, it is reasonable to directly compare position with time and, therefore, analyze the cooling rate from the chart. The temperature drops faster during the first block due to the water cooling system which strongly acts in the dome chamber. When the position reaches a certain point above this dome chamber, the water cooling loses impact and the temperature decreases more steadily. Furthermore, the very high temperature in the first positions of the ingot is mainly justified by the high radiation heat, which continuously loses its impact for positions from the melt interface.

Taking the first two position points, it is possible to observe a considerably different resistivity variation values, and, that is, thermal donor concentration. By knowing that most thermal donors, especially OTD, form at the temperature range of 300 ºC and 500 ºC, and that both points are above this range, this difference is mostly justified by the different oxygen levels, which greatly affect the [TD].

For the last two position points, it is possible to observe low resistivity variation values. Although the fifth position presents an higher resistivity variation than the forth position, it is in fact accordingly to the oxygen values but, nonetheless, carbon and metallic impurities affect the thermal donor concentration, which complicate thermal donor concentration estimations for such low resistivity variation values, which are usual in the last positions of most crystals.

12. Conclusion

Twenty-five ingots were studied, through 5 different samples from each ingot, and were characterized in terms of oxygen concentration, carbon concentration and resistivity, both before and after heat treatment.

There has been found a clear correlation between the resistivity variation, sample position and oxygen concentration, as according to the literature, for the samples studied. Nonetheless, sample characterization proved that the assumptions required are not perfectly met, as very different oxygen concentration values were found for the same position and resistivity variation value.

A model has been created and applied to both the whole sample set, with major differences that led to two different results, plus an additional application of the model to a smaller sample set. The model predicted oxygen concentration values with an accuracy above 90%. It is important to refer that the model failed to fit the oxygen concentration trend for every single ingot.

NorSun's heat treatment procedure has been compared to NTNU's heat treatment procedure, leading to interesting results, as the resistivity variation with NorSun's heat treatment is higher, along with a higher oxygen concentration reduction. Although a higher resistivity variation may mean a more effective thermal donor killing, the oxygen concentration reduction may lead to the formation of other oxygen compounds that alter wafer characteristics in an, at the moment, unknown way.

To summarize, through statistical analysis and modeling, it is possible to develop a model that provides oxygen concentration values, avoiding the utilization of measuring equipment such as FTIR, leading to faster and cheaper quality control.

13. Further Work

The results of the model greatly depend of the batch quality and size, as, for the model to have an acceptable performance, the assumptions previously considered must be respected, i.e. the thermal history of the different studied ingots must be as similar as possible and the heat treatment has to be as effective as possible. For more solid results, a larger sample set should be statistical analyzed, along with a deep understanding of the pulling parameters and equipment characteristics.

Only two pairs of ingots have been produced with the exact same run parameter, using the same puller and, due to the small number of samples, no reasonable conclusion could be found. Nonetheless, even using only samples with the sample pulling parameters and the same puller, one must consider how many ingots were produced in a row without changing the graphite hot zone, as the continuous use will lead to considerably different thermal histories.

Although these improvements do not seem simple, there is a very interesting point that should be mentioned, for further work. Since the whole point of this alternative method is, in fact, the time and cost reduction of the quality control procedure, reducing the number of measures and steps needed for the application of this model may be beneficial. As it is at the moment, alongside the position values of each sample, two measures of resistivity are required. An oxygen concentration value will be retrieved, considering the general behavior of the previous samples, but generally the oxygen concentration value is accurate in a strict position range.

Nonetheless, it may be possible to apply the Scheil's Equation to the model, leading to a single required resistivity measure, from a wafer near the seed or near the tail, to predict the oxygen concentration along a whole ingot, greatly reducing the quality control effort. In fact, this point has been tested for the sample set that has been studied during this work, but the comparison between the predicted resistivity values and the measured ones after the application of the Scheil's Equation were not good enough to retrieve accurate oxygen concentration values through the model. The model can be improved by including this point and, ultimately, achieve a good quality control process for the Czochralski industry.

14. References

[1] Association, Solar, 2015, Solar Industry Facts and Figures. SEIA [online]. 2015. [Accessed November 2015]. Available from: http://www.seia.org/research-resources/solar-industry-data

[2] Klitkou, Antje and Godoe, Helge, 2013, The Norwegian PV manufacturing industry in a Triple Helix perspective. Energy Policy. 2013. Vol. 61, p. 1586-1594. DOI 10.1016/j.enpol.2013.06.032. Elsevier BV

[3] Li, Sheng S, 2006, Semiconductor physical electronics. New York: Springer.

[4] Brain, Marshall, 2001, How Semiconductors Work. HowStuffWorks [online]. 2001. [Accessed September 2015]. Available from: http://electronics.howstuffworks.com/diode.htm

[5] Department of Microelectronics and Computer Engineering, 2008, The Semiconductor In Equilibrium. 1. TUDelft.

[6] Nsspi.tamu.edu, 2015, Introduction | Nuclear Security & Safeguards Education Portal. [Online]. 2015. [Accessed November 2015]. Available from: http://nsspi.tamu.edu/nssep/courses/basic-radiation-detection/semiconductor-detectors/introduction/introduction

[7] Sze, S. M, 1981, Physics of semiconductor devices. New York: Wiley.

[8] Bathey, B. R. and Cretella, M. C., 1982, Solar-grade silicon. J Mater Sci. 1982. Vol. 17, no. 11, p. 3077-3096. DOI 10.1007/bf01203469. Springer Science + Business Media

[9] https://www.mersen.com/uploads/pics/insulation-siemens-process-mersen_07.jpg

[10] http://2.bp.blogspot.com/-Sz-lKzyoE5A/U4xObUBpIyI/AAAAAAAAAfI/lMU0WTMo4Tc/s1600/mono-v-poly-crystalline-cells1.jpg

[11] http://jhaj.net/jasjeet/tcad/Learn1/l1k_files/image001.gif

[12] http://www.topsil.com/media/56109/fz_proces.jpg

[13] Ecee.colorado.edu, 2015, Carrier densities. [Online]. 2015. [Accessed October 2015]. Available from: http://ecee.colorado.edu/~bart/book/book/chapter2/ch2_6.htm

[14] Dhanaraj, Govindhan, 2010, *Springer handbook of crystal growth*. Heidelberg: Springer.

[15] Eranna, G, [no date], *Crystal growth and evaluation of silicon for VLSI and ULSI*.

[16] Markov, Ivan V, 2003, *Crystal growth for beginners*. Singapore : World Scientific.

[17] Nakajima, K and Usami, Noritaka, 2009, *Crystal growth of Si for solar cells*. Berlin: Springer Verlag.

[18] Pimpinelli, Alberto and Villain, Jacques, 1998, *Physics of crystal growth*. Cambridge: Cambridge University Press.

[19] Scheel, Hans J and Fukuda, Tsuguo, 2003, *Crystal growth technology*. Chichester, West Sussex: J. Wiley.

[20] Zulehner, Werner, 2000, Historical overview of silicon crystal pulling development. *Materials Science and Engineering: B*. 2000. Vol. 73, no. 1-3, p. 7-15. DOI 10.1016/s0921-5107(99)00427-4. Elsevier BV

[21] Tfssolar.co.za, 2015, [online]. 2015. [Accessed November 2015]. Available from: http://www.tfssolar.co.za/images/tfsmanufact/800px-Czochralski_Process.svg.png

[22] Luque, A and Hegedus, Steven, 2003, *Handbook of photovoltaic science and engineering*. Hoboken, NJ: Wiley.

[23] Goetzberger, A, Knobloch, Joachim and Voss, Bernhard, 1998, *Crystalline silicon solar cells*. Chichester : Wiley.

[24] Haunschild, Jonas, Broisch, Juliane, Reis, Isolde and Rein, Stefan, 2011, Quality Control of Czochralski grown silicon wafers in solar cell production using photoluminescence imaging.*26th PV Solar Energy Conference and Exhibition*. 2011.

[25] Paloheimo, Jari, 2015, *Silicon as MEMS Material*. 1.

[26] Páscoa, Soraia, 2014, *oxygen and related defects in Czochralski silicon crowns*

[27] Hu, Yu, 2012, *Characterization of Defects in N-type Cz Silicon for Solar Cells*. Philosophiae Doctor. Faculty of Natural Science and Technology, Norwegian University of Science and Technology.

[28] Zhang, Weilian, Yan, Shuxia and Ji, Zhijiang, 1996, Effective segregation coefficient and steady state segregation coefficient of germanium in Czochralski silicon. *Journal of Crystal Growth*. 1996. Vol. 169, no. 3, p. 598-599. DOI 10.1016/s0022-0248(96)00672-0. Elsevier BV

[29] ASTM, 2015, *Standard Practice for Conversion Between Resistivity and Dopant Density for Boron-Doped, Phosphorus-Doped, and Arsenic-Doped Silicon*. 1.

[30] Shimura, Fumio, 1994, *oxygen in silicon*. Boston : Academic Press.

[31] Newman, R C, 2000, oxygen diffusion and precipitation in Czochralski silicon. *Journal of Physics: Condensed Matter*. 2000. Vol. 12, no. 25, p. R335-R365. DOI 10.1088/0953-8984/12/25/201. IOP Publishing

[32] Yang, Deren, Li, Dongsheng, Wang, Lirong, Ma, Xiangyang and Que, Duanlin, 2002, oxygen in Czochralski silicon used for solar cells. *Solar Energy Materials and Solar Cells*. 2002. Vol. 72, no. 1-4, p. 133-138. DOI 10.1016/s0927-0248(01)00158-1. Elsevier BV

[33] Rafi, J. M., Simoen, E., Claeys, C., Ulyashin, A. G., Job, R., Fahrner, W. R., Versluys, J., Clauws, P., Lozano, M. and Campabadal, F., 2015, *Analysis of oxygen Thermal Donor Formation in n-type Cz Silicon*. 1. Barcelona: Institut de Microelectrònica de Barcelona.

[34] Puzanov, N I and Eidenzon, A M, 1992, The effect of thermal history during crystal growth on oxygen precipitation in Czochralski-grown silicon. *Semiconductor Science and Technology*. 1992. Vol. 7, no. 3, p. 406-413. DOI 10.1088/0268-1242/7/3/022. IOP Publishing

[35] Bruzzi, Mara, Menichelli, David, Scaringella, Monica, Härkönen, Jaakko, Tuovinen, Esa and Li, Zheng, 2006, Thermal donors formation via isothermal annealing in magnetic Czochralski high resistivity silicon. *J. Appl. Phys*. 2006. Vol. 99, no. 9, p. 093706. DOI 10.1063/1.2192307. AIP Publishing

[36] Emtsev, Valentin V., Oganesyan, Gagik A. and Schmalz, K., 1993, oxygen-Related Thermal Donors in Heat-Treated Cz-Si. *Defect and Diffusion Forum*. 1993. Vol. 103-105, p. 505-516. DOI 10.4028/www.scientific.net/ddf.103-105.505. Trans Tech Publications

[37] American Society for Testing and Materials, 2015, *Standard Test Method for Substitutional Atomic carbon COntent of Silicon by Infrared Absorption*. 1.

[38] Pveducation.org, [no date], Four Point Probe Resistivity Measurements | PVEducation. [Online]. [Accessed October 2015]. Available from: http://www.pveducation.org/pvcdrom/characterisation/four-point-probe-resistivity-measurements

[39] 4dimensions.com, [no date], Four Dimensions Inc. [online]. [Accessed October 2015]. Available from: http://www.4dimensions.com/b_4p.html

[40] Four Point Probes, 2013, Four-Point Probe Manual. [Online]. 2013. [Accessed November 2015]. Available from: http://four-point-probes.com/four-point-probe-manual/

[41] Newport.com, 2015, Introduction to FTIR Spectroscopy. [Online]. 2015. [Accessed November 2015]. Available from: http://www.newport.com/Introduction-to-FTIR-Spectroscopy/405840/1033/content.aspx

[42] Hyperphysics.phy-astr.gsu.edu, 2015, The Fermi-Dirac Distribution. [Online]. 2015. [Accessed October 2015]. Available from: http://hyperphysics.phy-astr.gsu.edu/hbase/quantum/disfd.html

[43] Pt.slideshare.net, 2009, Quantitative Analysis from Ftir. [Online]. 2009. [Accessed September 2015]. Available from: http://pt.slideshare.net/guest824336/quantitative-analysis-from-ftir

[44] PIKE TECHNOLOGIES, PIKE, [no date], *MAP300 Automated Wafer Analysis System Installation and User guide*. 1.

[45] Hyperphysics.phy-astr.gsu.edu, 2015, Table of Resistivity. [online]. 2015. [Accessed November 2015]. Available from: http://hyperphysics.phy-astr.gsu.edu/hbase/tables/rstiv.html
[46] SEMI, 2015, *Standard Test Method of Interstitial Atomic oxygen Content of Silicon by Infrared Absorption*. 1.
[47] SEMI, 2015, Guide to conversion factors for interstitial oxygen in Silicon. . 2015.
[48] SEMI, 2015, *Standard Test Methods for Resistivity of Semiconductor Materials*. 1.
[49] Fuller, Wayne A, 1987, *Measurement error models*. New York [etc.]: John Wiley.
[50] Hauser, John R, 2009, *Numerical methods for nonlinear engineering models*. Dordrecht: Springer.
[51] Chiang, Chin Long, 2003, *Statistical methods of analysis*. River Edge, N.J.: World Scientific.
[52] Freund, Rudolf J, Wilson, William J and Sa, Ping, 2006, *Regression analysis*. Burlington, MA: Elsevier Academic Press.
[53] Cameron, A. Colin, 2009, EXCEL Multiple Regression. *Cameron.econ.ucdavis.edu* [online]. 2009. [Accessed September 2015]. Available from: http://cameron.econ.ucdavis.edu/excel/ex61multipleregression.html
[54] ThermoNicole, Fourier Transform Infrared Spectrometry (2015), http://mmrc.caltech.edu/FTIR/FTIRintro.pdf

15. Appendix

Position Group	T0	T1	T2	T3	T4	T5
Min L	18,00	395,00	790,00	1185,00	1580,00	1873,00
Max L	40,00	435,00	830,00	1225,00	1620,00	1995,00
L Amp	22,00	40,00	40,00	40,00	40,00	122,00
Thickness Min	-	1,43	1,25	1,36	1,39	1,15
Thickness Max	-	2,29	1,78	2,08	2,31	1,98
Thickness Amp	-	0,86	0,53	0,72	0,92	0,83
Min ρ BHT	-	3,17	3,43	4,26	3,90	3,53
Max ρ BHT	-	6,51	7,04	6,02	5,60	5,68
ρ Amp BHT	-	3,35	3,61	1,76	1,70	2,15
Min ρ AHT	9,17	8,11	7,14	6,10	4,43	3,61
Max ρ AHT	13,37	10,20	8,70	7,40	5,95	5,53
ρ Amp AHT	4,20	2,09	1,55	1,30	1,53	1,92
Min Var ρ	-	2,69	0,52	1,08	0,09	0,02
Max Var ρ	-	5,94	4,76	2,87	1,73	1,16
Var ρ Amp	-	3,25	4,25	1,78	1,64	1,15
Min [Oi] BHT	-	10,07	9,46	8,57	8,77	7,84
Max [Oi] BHT	-	12,85	11,99	10,82	10,80	12,19
[Oi] Amp BHT	-	2,78	2,53	2,25	2,04	4,35
Min [Oi] AHT	11,99	8,50	7,70	6,74	7,15	6,75
Max [Oi] AHT	18,15	13,06	12,43	11,24	10,49	10,73
[Oi] Amp AHT	6,15	4,56	4,73	4,51	3,35	3,98
Min [C] BHT	-	0,31	0,31	0,36	0,39	0,48
Max [C] BHT	-	0,69	0,64	0,79	0,93	1,41
[C] Amp BHT	-	0,39	0,33	0,43	0,54	0,94
Min [C] AHT	0,00	0,24	0,33	0,25	0,47	0,55
Max [C] AHT	0,54	0,83	0,85	1,05	1,24	2,04
[C] Amp AHT	0,54	0,59	0,52	0,79	0,78	1,49

Table 3: Minimum, maximum and amplitude values for the complete data set.

FTIR BHT NTNU	Thickness	O	C
T1	1,45	16,3939	0,229
T5	1,45	12,28	0
FTIR AP	Thickness	Oi	C
T1-1	1,4273	16,2	0,6365
T1-2	1,433	16,1485	0,4962
T1-3	1,4328	16,1154	0,2164
AvgT1	1,4310	16,1546	0,4497
T5-1	1,3686	11,9875	0,5762
T5-2	1,375	12,03	0,6435
T5-3	-	11,9	0,6802
AvgT5	1,3718	11,9725	0,6333

NTNU FTIR AHT	Thickness	Oi	C
T1-1	1,3958	16,2211	0,3908
T1-2	1,3876	16,2663	0,4567
T1-3	1,3779	16,0969	0,1986
AvgT1	1,3871	16,19476667	0,3487
T5-1	1,3452	12,2103	0,4639
T5-2	1,3411	12,062	0,4087
T5-3	1,3349	12,0275	0,6732
AvgT5	1,3404	12,0999	0,5152
FPP BHT NTNU	mV	FPP AP NTNU	mV
T1-1	15,46	T1-1	15,4
T1-2	15,56	T1-2	15,62
T1-3	15,4	T1-3	15,85
T1-4	15,25	T1-4	15,44
T1-5	15,23	T1-5	15,03
AvgT1	15,38	AvgT1	15,468
T5-1	13,46	T5-1	13,87
T5-2	13,61	T5-2	13,9
T5-3	14,1	T5-3	13,93
T5-4	13,92	T5-4	14,01
T5-5	13,96	T5-5	13,9
AvgT5	13,81	AvgT5	13,922
FPP AHT NTNU	mV	FPP AHT NorSun	mV
T1-1	18,3	T1-1	21,55
T1-2	18,47	T1-2	22,25
T1-3	22,02	T1-3	23,6
T1-4	20,51	T1-4	22,62
T1-5	18,41	T1-5	21,39
AvgT1	19,542	AvgT1	22,282
T5-1	14,42	T5-1	14,04
T5-2	14,03	T5-2	14,04
T5-3	13,95	T5-3	14,17
T5-4	14,64	T5-4	13,99
T5-5	14,23	T5-5	14,17
AvgT5	14,254	AvgT5	14,082
NorSun FTIR AHT	Thickness	Oi	C
T5-1	1,151	16,145	0,3938
T5-2	1,114	16,0811	0,3846
T5-3	1,3094	15,9699	0,354
AvgT1	1,1914	16,0653	0,3774
T1-1	1,3513	12,058	0,5624
T1-2	1,3608	11,9549	0,5743
T1-3	1,3664	11,8834	0,6022
AvgT5	1,3595	11,9654	0,5796

Table 4: Data acquired to compare heat treatment performances. AP stands for After Polishing.

Base model: [Oi] vs Position 2183A

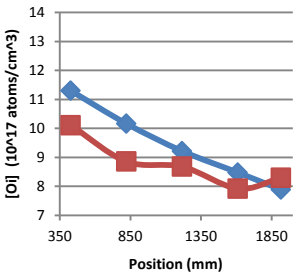

Base model: [Oi] vs Position 2721B

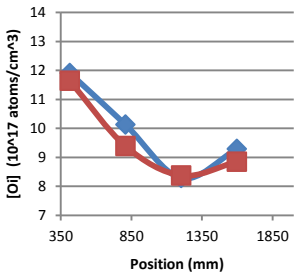

Base model: [Oi] vs Position 2466A

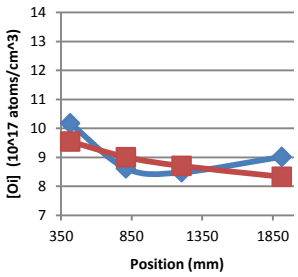

Base model: [Oi] vs Position 2718B

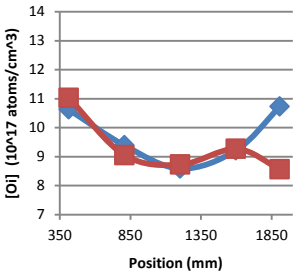

Base model: [Oi] vs Position 2812A

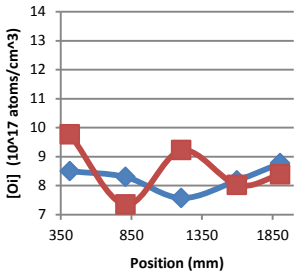

Base model: [Oi] vs Position 2733B

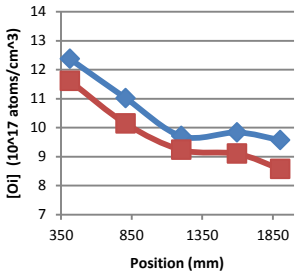

Base model: [Oi] vs Position 2466B

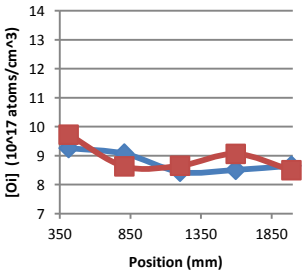

Base model: [Oi] vs Position 2381B

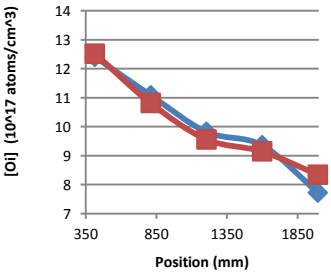

Base model: [Oi] vs Position 2412A

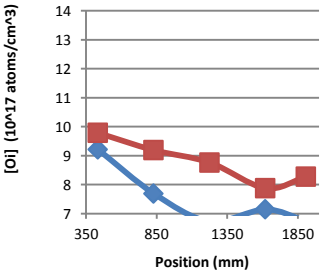

Base model: [Oi] vs Position 5156A

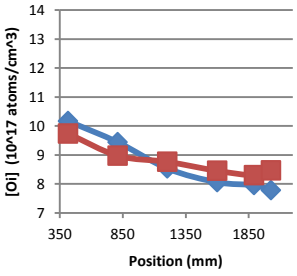

Base model: [Oi] vs Position 2377B

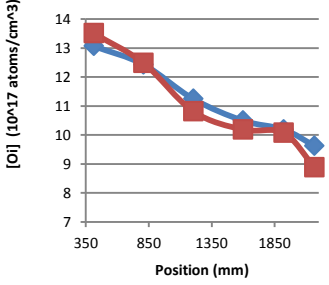

Base model: [Oi] vs Position 2412B

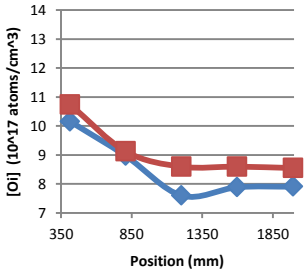

Base model: [Oi] vs Position 2091A

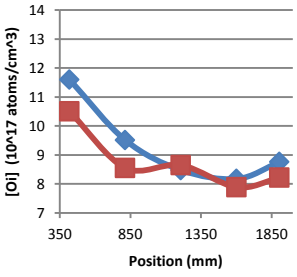

Base model: [Oi] vs Position 2471A

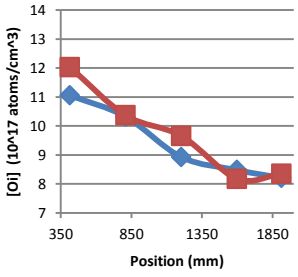

Base model: [Oi] vs Position 2193A

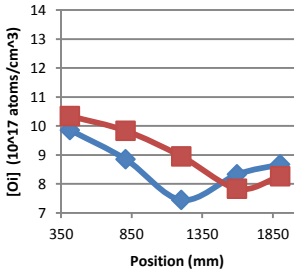

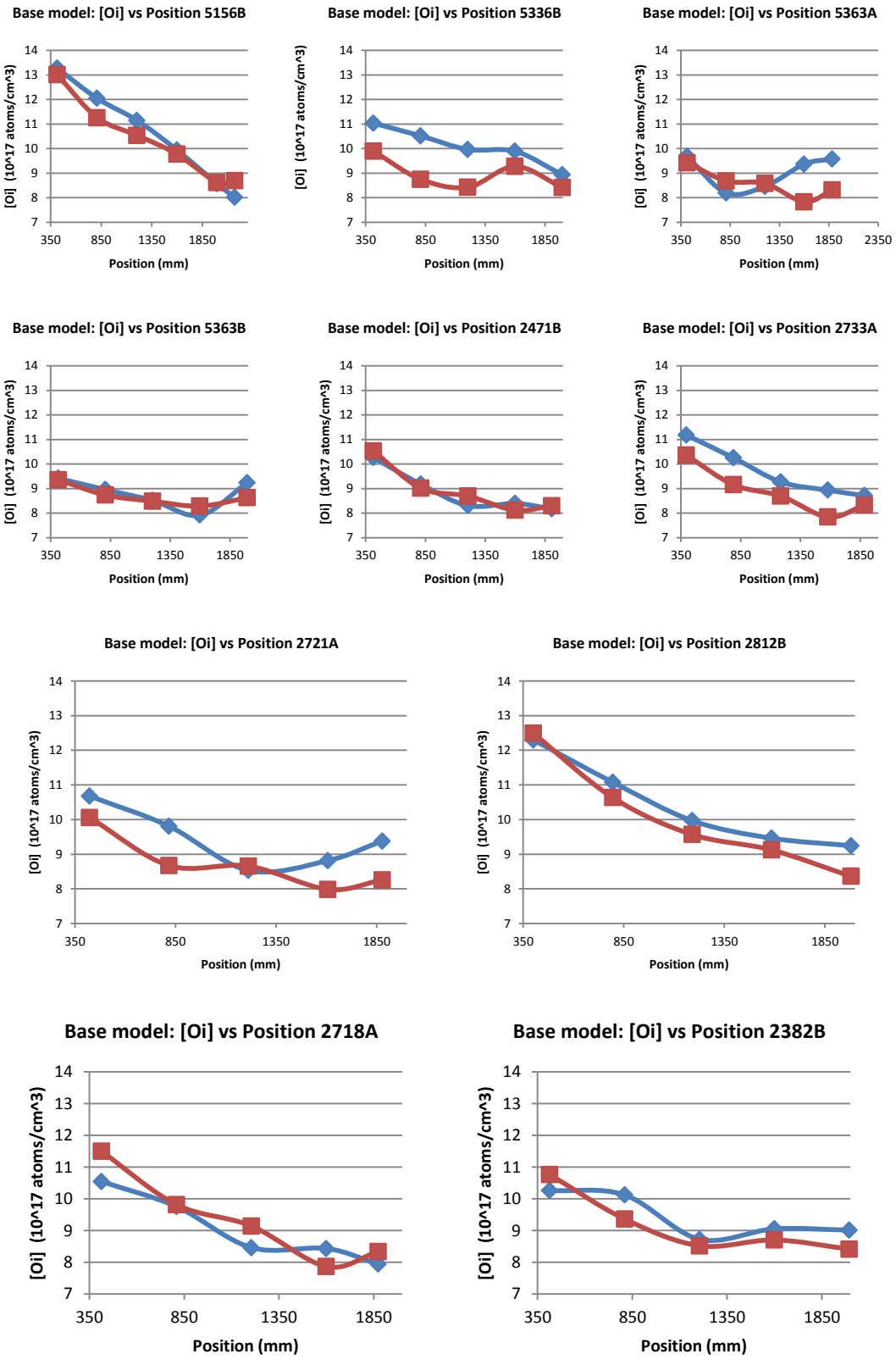

Figure 69: Base model results. Red lines represent estimated values and blue lines measured values.

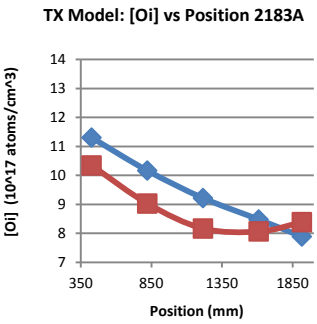
TX Model: [Oi] vs Position 2183A
[Oi] (10^17 atoms/cm^3)
Position (mm)

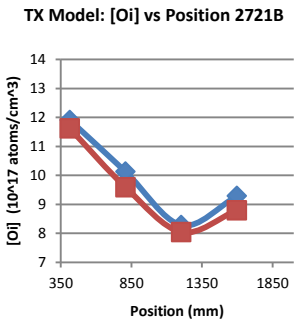
TX Model: [Oi] vs Position 2721B
[Oi] (10^17 atoms/cm^3)
Position (mm)

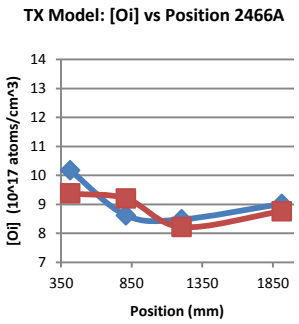
TX Model: [Oi] vs Position 2466A
[Oi] (10^17 atoms/cm^3)
Position (mm)

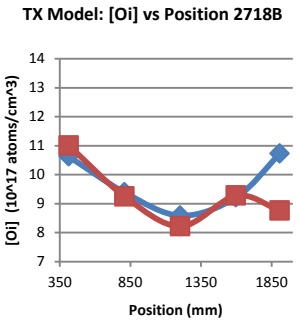
TX Model: [Oi] vs Position 2718B
[Oi] (10^17 atoms/cm^3)
Position (mm)

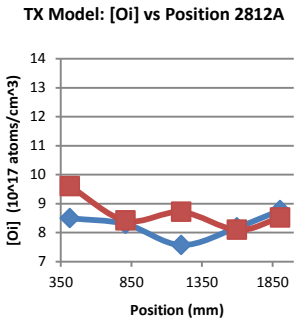
TX Model: [Oi] vs Position 2812A
[Oi] (10^17 atoms/cm^3)
Position (mm)

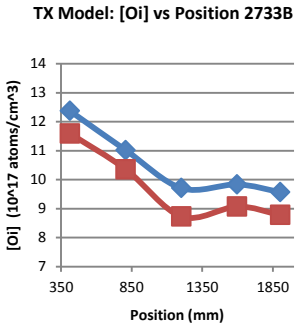
TX Model: [Oi] vs Position 2733B
[Oi] (10^17 atoms/cm^3)
Position (mm)

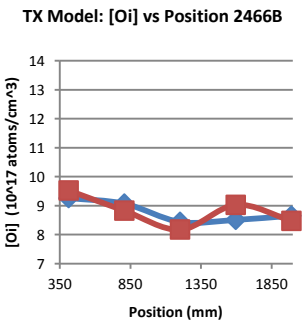
TX Model: [Oi] vs Position 2466B
[Oi] (10^17 atoms/cm^3)
Position (mm)

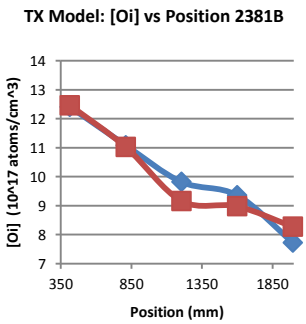
TX Model: [Oi] vs Position 2381B
[Oi] (10^17 atoms/cm^3)
Position (mm)

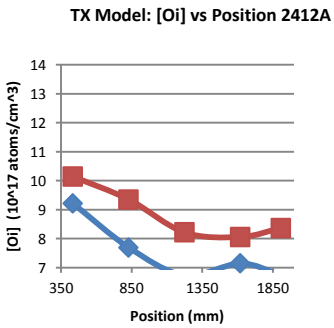
TX Model: [Oi] vs Position 2412A
[Oi] (10^17 atoms/cm^3)
Position (mm)

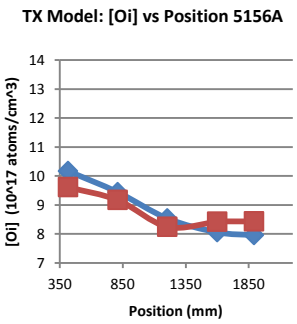
TX Model: [Oi] vs Position 5156A
[Oi] (10^17 atoms/cm^3)
Position (mm)

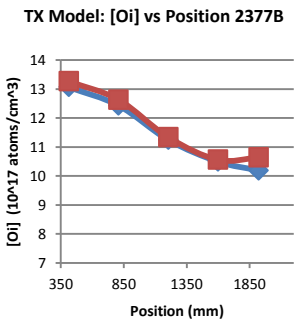
TX Model: [Oi] vs Position 2377B
[Oi] (10^17 atoms/cm^3)
Position (mm)

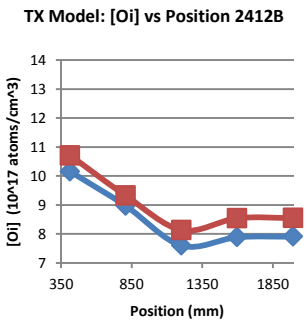
TX Model: [Oi] vs Position 2412B
[Oi] (10^17 atoms/cm^3)
Position (mm)

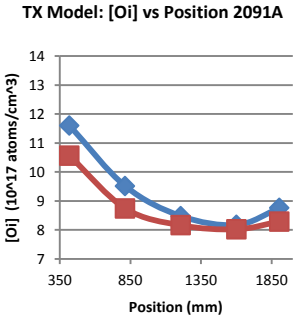
TX Model: [Oi] vs Position 2091A
[Oi] (10^17 atoms/cm^3)
Position (mm)

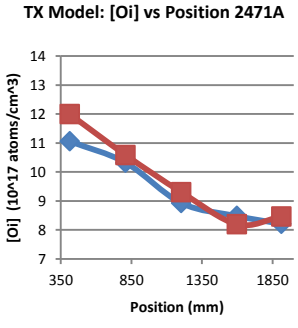
TX Model: [Oi] vs Position 2471A
[Oi] (10^17 atoms/cm^3)
Position (mm)

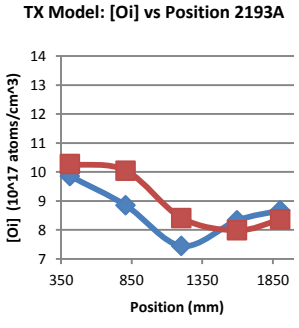
TX Model: [Oi] vs Position 2193A
[Oi] (10^17 atoms/cm^3)
Position (mm)

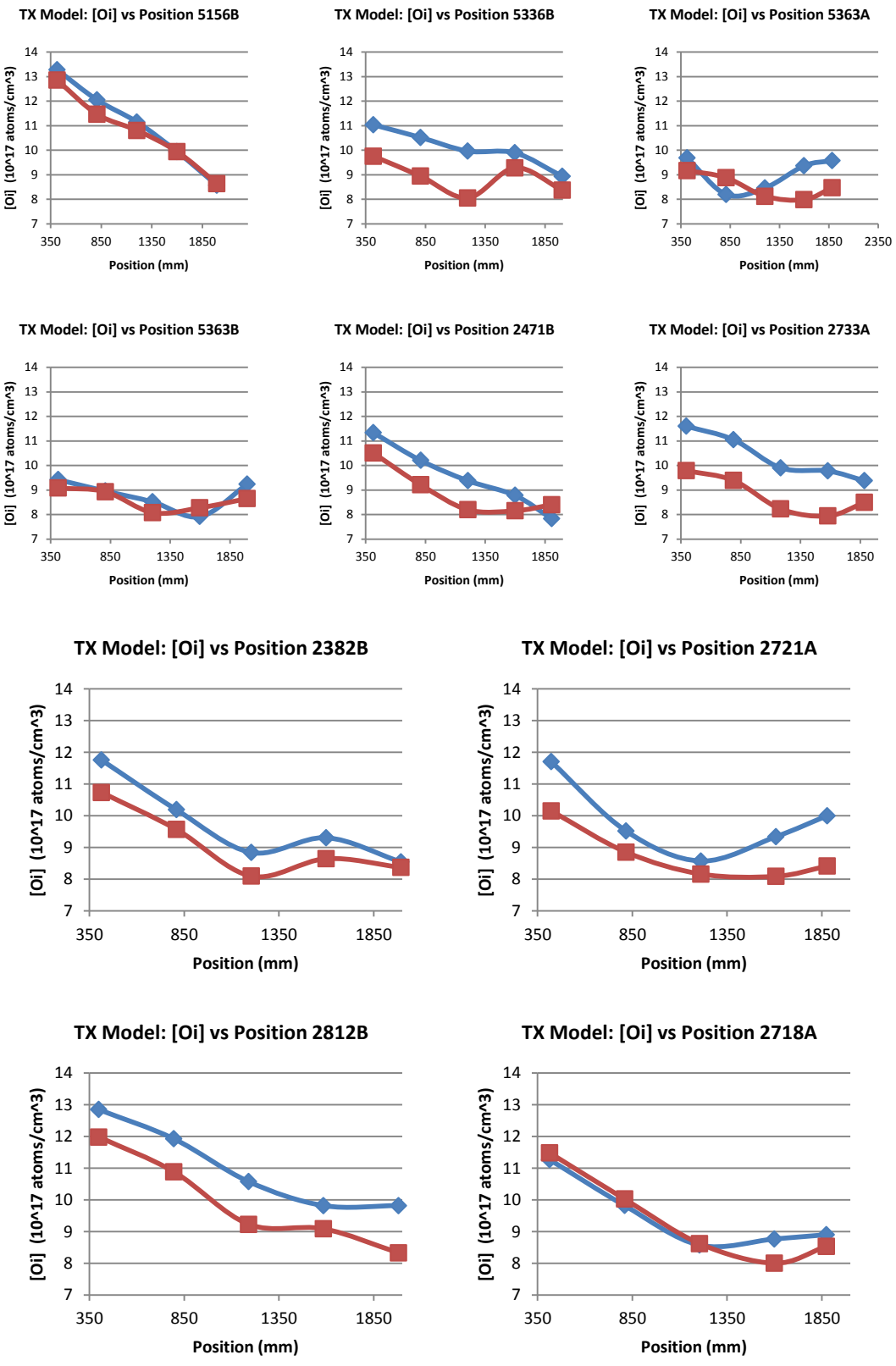

Figure 70: TX model results. Red lines represent estimated values and blue lines measured values.

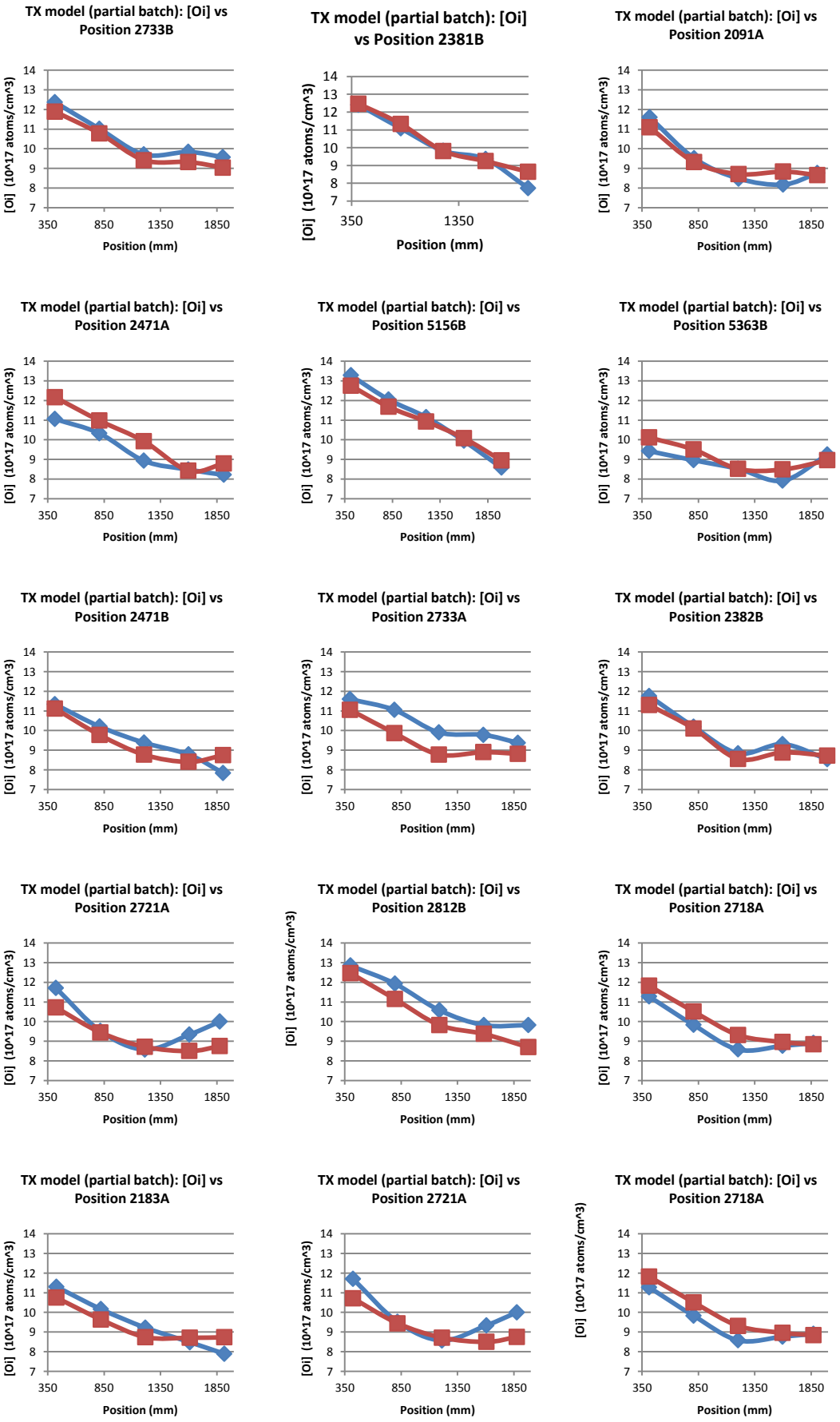

Figure 71: TX model results (partial batch). Red lines represent estimated values and blue lines measured values.

Code	Puller	Run ID	Sample	Position	L	varρ	[Oi] AHT	[C] AHT
Average values	-	-	T0	21	-	-	16,2053	0,3226
	-	-	T1	415	1,5576	3,9645	10,8117	0,4850
	-	-	T2	810	1,5362	2,5913	9,7956	0,5328
	-	-	T3	1205	1,5876	1,5648	8,8176	0,6037
	-	-	T4	1600	1,5935	0,5676	8,8476	0,7763
	-	-	T5	1935	1,5640	0,0731	8,7363	0,9954
	-	-	T6	2216	-	-	8,9554	1,3784
Ingot 2183A	51	29	T0	32	-	-	15,2207	0,4621
			T1	427	1,4832	3,4712	11,3000	0,4641
			T2	822	1,5941	2,1360	10,1631	0,5606
			T3	1217	1,3594	1,3165	9,2157	0,5983
			T4	1612	1,5224	0,1415	8,4776	0,8271
			T5	1917	1,8321	0,0708	7,8883	1,1370
			T6	2196	-	-	9,2589	1,4354
Ingot 2721B	70	34	T0	19	-	-	18,0529	0,3448
			T1	414	1,5151	4,6934	11,9050	0,5777
			T2	809	1,5219	2,6159	10,1269	0,4460
			T3	1204	1,5243	1,0848	8,2860	0,4976
			T4	1599	1,5037	0,8493	9,2866	0,8222
			T5	1994	1,5094	-1,9132	8,7935	1,0898
			T6	2406	-	-	8,9824	0,3448
Ingot 2466A	61	32	T0	21	-	-	16,4736	0,3598
			T1	416	1,4974	2,8931	10,1702	0,3150
			T2	811	1,4927	2,2903	8,6204	0,4187
			T3	1206	1,4974	1,3540	8,4837	0,4731
			T4	1601	1,5055	-0,5044	9,5369	0,5421
			T5	1916	1,4940	0,0921	9,0205	0,6080
			T6	2184	-	-	8,0668	0,7936
Ingot 2718B	53	35	T0	19	-	-	15,7161	0,3711
			T1	414	1,5148	4,2207	10,6237	0,5427
			T2	809	1,5001	2,3325	9,3858	0,5653
			T3	1204	1,5181	1,3759	8,5892	0,6454
			T4	1599	1,5146	1,1352	9,2193	0,8158
			T5	1909	1,5297	0,2550	10,7281	1,1197
			T6	2294	-	-	12,9849	1,8613
Ingot 2812A	56	37	T0	19	-	-	15,1256	0,3488
			T1	414	1,5061	3,1148	8,4994	0,3897
			T2	809	1,5307	0,5156	8,2975	0,4851
			T3	1204	1,5202	1,7632	7,5740	0,4493
			T4	1599	1,5163	0,2360	8,1811	0,5302
			T5	1905	1,4538	0,1380	8,7711	0,5774
			T6	2171	-	-	7,8836	0,7928

Ingot 2733B	51	36	T0	19	-	-	15,6270	0,5306
			T1	414	1,5147	4,6703	12,3665	0,6354
			T2	809	1,5276	3,2089	11,0138	0,6125
			T3	1204	1,4968	1,7725	9,7066	0,8375
			T4	1599	1,5037	1,0194	9,8366	0,9271
			T5	1905	1,5255	0,2642	9,5719	1,2624
			T6	2231	-	-	9,8619	2,5272
Ingot 2466B	61	32	T0	18	-	-	16,3490	0,4852
			T1	413	1,5138	3,0682	9,2606	0,5554
			T2	808	1,4881	1,9484	9,0681	0,4822
			T3	1203	1,4913	1,3209	8,4394	0,6499
			T4	1598	1,5021	0,9955	8,5104	0,7081
			T5	1993	1,5011	0,1149	8,6548	1,1679
			T6	2352	-	-	8,3361	2,1750
Ingot 2381B	55	32	T0	20	-	-	17,3105	0,5020
			T1	415	1,4936	5,3116	12,4077	0,8323
			T2	810	1,5023	3,6912	11,0818	0,7359
			T3	1205	1,4916	2,0141	9,8185	1,0452
			T4	1600	1,5022	1,0483	9,3568	1,2430
			T5	1995	1,5023	0,0173	7,7250	2,0379
			T6	2343	-	-	9,6882	4,0236
Ingot 2412A	56	32	T0	40	-	-	14,1665	0,2493
			T1	435	1,4985	3,1799	9,2125	0,2428
			T2	830	1,4872	2,4164	7,6950	0,3303
			T3	1225	1,4916	1,3720	6,7358	0,4352
			T4	1620	1,5017	0,0978	7,1466	0,5818
			T5	1908	1,4965	0,0610	6,7452	0,8062
			T6	2195	-	-	8,0210	0,8866
Ingot 5156A	54	65	T0	21	-	-	17,1223	0,3772
			T1	416	1,4854	3,0870	10,1677	0,4815
			T2	811	1,6076	2,2579	9,4377	0,4991
			T3	1206	1,5784	1,4015	8,5310	0,6114
			T4	1601	1,7163	0,5585	8,0594	0,8644
			T5	1894	1,7093	0,0954	7,9596	0,9183
			T6	2028	1,4058	0,0632	7,7743	1,1585
			T7	2162	-	-	8,6717	0,5408
Ingot 2377B	48	31	T0	19	-	-	18,0519	0,3999
			T1	414	1,5135	5,9396	13,0612	0,4821
			T2	809	1,5335	4,7632	12,4284	0,5567
			T3	1204	1,5307	2,8685	11,2425	0,6465
			T4	1599	1,5381	1,7256	10,4935	0,8523
			T5	1922	1,5277	1,1625	10,1903	1,0781
			T6	2167	1,5403	0,1719	9,6264	1,4591
			T7	2432	-	-	10,7342	3,0946

Ingot 2412B	56	32	T0	19	-	-	15,7678	0,4377
			T1	414	1,5393	3,9917	10,1567	0,6757
			T2	809	1,5168	2,3910	8,9665	0,5382
			T3	1204	1,5260	1,2702	7,5994	0,6892
			T4	1599	1,5429	0,6667	7,8885	0,9035
			T5	1994	1,5308	0,1512	7,9078	1,0091
			T6	2285	-	-	7,7412	2,1109
Ingot 2091A	51	28	T0	23	-	-	15,2076	0,4205
			T1	418	2,2872	3,8023	11,6034	0,4126
			T2	813	1,2471	1,8690	9,5161	0,5813
			T3	1208	2,0807	1,3067	8,4790	0,6402
			T4	1603	2,3055	0,1232	8,1758	0,9466
			T5	1906	1,9807	0,0261	8,7587	1,1189
			T6	2176	-	-	7,5098	1,3149
Ingot 2471A	70	31	T0	19	-	-	17,0092	0,4956
			T1	414	1,5372	4,9769	11,0562	0,4476
			T2	809	1,5187	3,3786	10,3213	0,4795
			T3	1204	1,5195	2,0846	8,9278	0,4824
			T4	1599	1,5159	0,3530	8,4804	0,5936
			T5	1913	1,5391	0,1102	8,2099	0,6660
			T6	2185	-	-	8,4921	0,8403
Ingot 2193A	56	30	T0	19	-	-	16,0333	0,3259
			T1	414	1,5680	3,6490	9,8567	0,3619
			T2	809	1,7262	2,9749	8,8472	0,5027
			T3	1204	1,9851	1,5532	7,4466	0,4795
			T4	1599	1,8914	0,0872	8,3306	0,4662
			T5	1904	1,7079	0,0600	8,6764	0,6834
			T6	2170	-	-	8,0179	0,7149
Ingot 5156B	54	65	T0	19	-	-	16,1102	0,3362
			T1	414	1,7040	5,6314	13,2747	0,5417
			T2	809	1,7794	3,9987	12,0468	0,6114
			T3	1204	1,9719	2,6920	11,1484	0,8518
			T4	1599	1,7794	1,4669	9,9410	0,9185
			T5	1994	1,5331	0,1958	8,5749	1,1618
			T6	2170	1,9085	0,0608	8,0181	1,5530
			T7	2346	-	-	12,0585	1,4054
Ingot 5336B	44	65	T0	19	-	-	16,7803	0,4491
			T1	414	1,5132	3,2386	11,0347	0,5846
			T2	809	1,5372	2,0625	10,5202	0,4226
			T3	1204	1,5751	1,1270	9,9649	0,6345
			T4	1599	1,6946	1,1389	9,8932	0,7812
			T5	1994	1,7479	0,0687	8,9397	0,7630
			T6	2157	1,3231	0,0364	8,5836	1,1766
			T7	2320	-	-	8,8825	1,9844

Ingot 5363A	8	76	T0	19	-	-	15,7207	0,3366
			T1	414	1,4273	2,7624	9,6834	0,4386
			T2	809	1,7122	1,9982	8,1983	0,6127
			T3	1204	1,8378	1,2581	8,4687	0,6411
			T4	1599	1,3880	0,0853	9,3675	0,8008
			T5	1885	1,8037	0,1152	9,5789	0,9010
			T6	2151	-	-	12,8839	0,8601
Ingot 5363B	8	76	T0	19	-	-	18,1461	0,4023
			T1	414	1,7166	2,6869	9,4204	0,4417
			T2	809	1,5158	2,0479	8,9565	0,5259
			T3	1204	1,5847	1,1784	8,5176	0,6795
			T4	1599	1,8407	0,4387	7,9173	0,9675
			T5	1994	1,3323	0,2004	9,2394	1,0902
			T6	2339	-	-	8,5306	2,0802
Ingot 2471B	70	31	T0	20	-	-	16,6522	0,0900
			T1	415	1,4912	3,8150	10,2648	0,6777
			T2	810	1,4978	2,3019	9,1799	0,6690
			T3	1205	1,4949	1,3520	8,3097	0,4467
			T4	1600	1,4838	0,3075	8,3939	0,9845
			T5	1907	1,1515	0,0795	8,1795	1,1045
			T6	2152	-	-	8,9740	1,6000
Ingot 2733A	51	36	T0	19	-	-	15,8788	0,1400
			T1	395	1,5184	3,6183	11,1796	0,3389
			T2	790	1,5316	2,4507	10,2527	0,6162
			T3	1185	1,5240	1,3866	9,2717	0,6619
			T4	1580	1,5292	0,1160	8,9349	0,7144
			T5	1887	1,5195	0,1269	8,7152	1,0465
			T6	2132	-	-	9,2421	0,9500
Ingot 2382B	53	32	T0	19	-	-	17,1323	0,0400
			T1	414	1,4867	4,0122	10,2635	0,4602
			T2	809	1,5008	2,5985	10,1233	0,5838
			T3	1204	1,5068	1,2065	8,7246	0,6119
			T4	1599	1,5023	0,7416	9,0518	0,6732
			T5	1994	1,5171	0,0641	9,0138	1,2321
			T6	2330	-	-	9,2448	1,5000
Ingot 2721A	70	34	T0	27	-	-	16,3939	0,0000
			T1	422	1,5291	3,4121	10,6787	0,3986
			T2	817	1,4992	1,9744	9,8072	0,4427
			T3	1212	1,5385	1,3069	8,5307	0,4972
			T4	1607	1,5066	0,1957	8,8147	0,5352
			T5	1878	1,5192	0,0837	9,3803	0,6317
			T6	2148	-	-	8,7045	0,4300

Ingot 2812B	**56**	**37**	T0	19	-	-	17,0914	0,1600
			T1	414	1,5681	5,2776	12,2989	0,5069
			T2	809	1,5170	3,5976	11,0788	0,6143
			T3	1204	1,5247	2,0479	9,9682	0,6324
			T4	1599	1,5112	1,0570	9,4622	0,8471
			T5	1994	1,6206	0,0458	9,2443	1,1223
			T6	2288	-	-	9,5953	1,4600
Ingot 2718A	53	39	T0	19	-	-	11,9933	0,0000
			T1	414	1,5179	4,5895	10,5463	0,3207
			T2	809	1,5196	2,9625	9,7565	0,4264
			T3	1204	1,5198	1,7050	8,4607	0,2548
			T4	1599	1,5189	0,1107	8,4345	0,5605
			T5	1873	1,5154	0,1418	7,9409	0,5519
			T6	2157	-	-	7,8634	0,4100

Table 5: Samples main data.